CANCER

Sphingolipid synthesis in tumor-associated macrophages confers immunotherapy resistance in hepatocellular carcinoma

Xiaozhen Zhang[1,2,3], Mengyi Lao[2,4], Kang Sun[1,2,3], Hanshen Yang[1,2,3], Lihong He[1,2,3], Xinyuan Liu[1,2,3], Linyue Liu[1,2,3], Sirui Zhang[1,2,3], Chengxiang Guo[2,5], Sicheng Wang[1,2,3], Jiatao Shi[1,2,3], Xiaoyu Zhang[1,2,3], Daqian Xu[1,2,3], Xiongbin Lu[1,2,3]*, Xueli Bai[1,2,3]*, Tingbo Liang[1,2,3]*

Dysregulated metabolism of immune cells in the tumor microenvironment leads to immune evasion and tumor progression. As a major cell component in the tumor, the metabolic reprogramming of tumor-associated macrophages (TAMs) creates an immunosuppressive microenvironment in hepatocellular carcinoma (HCC). Our study found that sphingolipid (particularly, sphingosine-1-phosphate or S1P) levels are a clinical indicator for prognosis and immunotherapy response in patients with HCC. S1P primarily derived from TAMs, where NIMA-related kinase 2 (NEK2) plays a key role in controlling the activity of serine palmitoyl-CoA transferase, a rate-limiting enzyme in S1P biosynthesis. The S1P produced by NEK2^{hi} TAMs promotes hepatic tumor progression and confers immunotherapy resistance. Targeting S1P synthesis with a NEK2 inhibitor or S1P antagonist disrupted the immunosuppressive function of macrophages, shifted regulatory T cells (T_{regs}) to T_H17 cells, and increased the number and activity of tumor-infiltrating T effectors, thereby enhancing antitumor efficacy in synergy with immune checkpoint blockade therapy.

INTRODUCTION

Hepatocellular carcinoma (HCC) is one of the leading causes of cancer-related deaths worldwide, accounting for more than three-quarters of a million deaths in 2022 (*1*). Increasing evidence shows that tumor-associated macrophages (TAMs) are a prominent component of the HCC microenvironment, contributing to hepatocarcinogenesis, therapy resistance, and poor clinical outcomes (*2*). TAMs are highly heterogeneous, displaying various subpopulations characterized by different origins, functions, and therapeutic potentials. Notably, TAMs generally polarize into two distinct phenotypes: immunosuppressive (M2) and proinflammatory (M1) macrophages. Most of the TAMs polarize toward an M2 phenotype, promoting HCC initiation, progression, and immunotherapy resistance through the secretion of protumor and proangiogenic factors and fostering an immunosuppressive environment. Conversely, M1 macrophages exhibit antitumor properties by releasing proinflammatory factors such as reactive oxygen species and interleukin-1β (IL-1β) (*3*, *4*). These insights suggest that selectively depleting TAM subpopulations or inducing a switch to the M1 phenotype could be a potential therapeutic strategy for inhibiting HCC progression and overcoming immunotherapy resistance.

Recent studies have provided clues into the immunometabolic regulation of TAMs. For instance, macrophages with high levels of cholesterol-25-hydroxylase (CH25H) are enriched in immunosuppressive subpopulations and are associated with poor survival rates in various types of cancer. Targeting CH25H disrupts macrophage immunosuppressive functions, enhancing the infiltration and activity of T cells, which, in combination with anti-programmed death-1 antibody (αPD-1), improves antitumor efficacy (*5*). Similarly, deletion of receptor-interacting protein kinase 3 (RIPK3) in TAMs facilitates fatty acid metabolism, including fatty acid oxidation (FAO), inducing M2 polarization. Up-regulation of RIPK3 or blockade of FAO reverses TAM immunosuppressive activity and disrupts HCC tumorigenesis (*6*). In addition, the PERK [protein kinase R-like endoplasmic reticulum (ER) kinase] signaling cascade in TAMs promotes immunosuppressive M2 activation and proliferation by up-regulating serine biosynthesis. PERK deficiency suppresses macrophage immunosuppressive activity and enhances the efficacy of immune checkpoint blockade (ICB) (*7*). Metabolites in the tumor microenvironment (TME), produced by tumor and immune cells, educate immune cells for the control of tumor development. However, knowledge about these critical metabolites in the TME that govern the fate of macrophages and their switch between immunosuppressive and immunostimulatory states is limited. In particular, it has been a challenge to identify metabolites as biomarkers for prognosis in clinical settings. In this study, we identified sphingosine-1-phosphate (S1P) in serum, a bioactive lipid molecule involved in multiple cellular signaling pathways and crucial for immune cell trafficking, as a potential prognostic indicator and predictor of immunotherapy response in HCC.

Previous studies on S1P have primarily focused on non-neoplastic diseases, highlighting its role in T cell migration from the thymus to the blood and from lymph nodes to lymphatics (*8*). Elevated S1P levels prolong T cell residence in lymph nodes, exacerbating conditions like experimental autoimmune encephalomyelitis (*9*). S1P metabolism is also critical in regulating fibrosis in organs such as the liver and heart (*10*, *11*). In colon tumors, sphingolipid synthesis translates extracellular metabolite availability into nuclear signals

[1]Department of Hepatobiliary and Pancreatic Surgery, the First Affiliated Hospital, School of Medicine, Zhejiang University, Hangzhou 310003, Zhejiang, China. [2]Zhejiang Provincial Key Laboratory of Pancreatic Disease, the First Affiliated Hospital, School of Medicine, Zhejiang University, Hangzhou 310009, Zhejiang, China. [3]MOE Joint International Research Laboratory of Pancreatic Diseases, Hangzhou, China. [4]Department of Breast, the First Affiliated Hospital, School of Medicine, Zhejiang University, Hangzhou 310003, Zhejiang, China. [5]Department of Oncology, the First Affiliated Hospital, School of Medicine, Zhejiang University, Hangzhou 310003, Zhejiang, China.
*Corresponding author. Email: liangtingbo@zju.edu.cn (T.L.); shirleybai@zju.edu.cn (X.B.); xiongbinlu@zju.edu.cn (X.L.)

for regulatory T cell (T_{reg}) differentiation, limiting antitumor immunity (*12*). In melanoma, S1P signaling activates peroxisome proliferator–activated receptor γ, skewing the T_{reg}/T helper cell 17 (T_H17) balance and limiting T cell–mediated antitumor responses (*13*). In mouse model of congestive hepatopathy, S1P promotes tumor development and metastasis as well as liver fibrosis (*14*). However, S1P metabolism and its contribution to the tumor immune microenvironment of HCC are largely unclear.

In this study, we demonstrated that levels of S1P and related metabolites, sphinganine and sphingomyelin (SM), are substantially higher in patients with HCC who are resistant to immunotherapy compared to responders. TAMs are identified as the main source of S1P-related metabolites, with never in mitosis gene A–related kinase 2 (NEK2) playing a key role in governing this metabolic pathway. $NEK2^{hi}$ TAMs drive immunotherapy resistance in HCC, leading to poor clinical outcomes. The S1P produced by $NEK2^{hi}$ TAMs promotes hepatic tumor progression and confers immunotherapy resistance through immunometabolic reprogramming. Mechanistically, NEK2 activates serine palmitoyl–coenzyme A transferase (SPT), a rate-limiting enzyme in the S1P biosynthesis pathway. Inhibition of NEK2 in combination with ICB eradicates HCC in humanized mouse tumor models. Our findings not only provide a clinical indicator of prognosis and immunotherapy response for HCC but also suggest a therapeutic strategy targeting TAM immunometabolism.

RESULTS

S1P metabolism is elevated in therapeutic resistance group of HCC

Metabolites in the TME reprogram functions of infiltrated immune cells and mediate cross-talks between tumor cells and stromal cells (*15*). Here, we first performed metabolomic analysis of the serum of patients with HCC in a clinical trial (NCT04174781), including the responder group [complete response (CR)/partial response (PR)], $n = 20$; and the nonresponder group [stable disease (SD)/progressive disease (PD)], $n = 10$. Representative images of responder group and nonresponder group were shown in Fig. 1A. This clinical study aimed to evaluate the efficacy and the safety of the anti–PD-1 sintilimab injection in combination with transarterial chemoembolization with drug-eluting beads (TACE-DEB) in patients with HCC beyond the Milan criteria. The clinical characteristics of patients are summarized in table S1. We found that the levels of S1P were the most substantially increased in serum of the nonresponder group compared with the responder group (Fig. 1B). We used an enzyme-linked immunosorbent assay (ELISA) assay to confirm this result in the serum of patients. The levels of S1P are much higher in the serum of nonresponder patients, while the intermediate metabolites, sphinganine and SM, showed no obvious difference, suggesting that S1P is a primary signaling metabolite secreted by the tumor tissue (Fig. 1C). Meanwhile, no substantial increase in S1P secretion was observed in patients before and after sintilimab therapy (Fig. 1D). We evaluated the reliability of S1P as a predictive model for immunotherapy response using ROC (receiver operating characteristic) curve analysis. The area under curve value of 0.9167 suggests that the model is highly effective at distinguishing between the responder and nonresponder groups. The chosen cutoff value of 1453 pg/ml provides a good balance between sensitivity (90.48%) and specificity (81.82%), making it a reliable threshold for classification in this context (Fig. 1E).

Next, we performed metabolomic analysis of human HCC tumors (the responder group, $n = 3$; the nonresponder group, $n = 3$; patient information in table S2) from humanized mouse HCC models treated with anti–PD-1 monoclonal antibody (sintilimab, 10 mg/kg, once a week, ip) (Fig. 1, F and G). As expected, we identified sphingolipid metabolism pathways with the most substantial change using Kyoto Encyclopedia of Genes and Genomes (KEGG) pathway enrichment analysis of responder group and nonresponder groups by liquid chromatography–mass spectrometry (LC-MS) proteomics (Fig. 1H). In the top-ranked metabolites that differ in the responder and nonresponder tumors, there are plasma membrane components, such as phosphatidylethanolamine and phosphatidylinositol, and oxidized DNA base FAPy-adenine, indicating tumor cell hyperproliferation and hypoxic TME. Levels of three major metabolites in the S1P biosynthesis pathway—C16 sphinganine, SM, and S1P—were substantially higher in the nonresponders compared to the responders (Fig. 1I).

In addition, we quantified the S1P levels in serum and tissue lysates of patients with HCC without immunochemotherapy and found that the up-regulated in S1P (but not the intermediate metabolites sphinganine and SM) is globally up-regulated in HCC samples compared to benign hepatic hemangiomas (Fig. 1J and fig. S1A). In both the hydrodynamic tail vein injection (HTVi) model and diethylnitrosamine-induced mouse HCC model, the levels of S1P were also markedly increased in HCC tumor tissues and mouse serum (fig. S1, B and C). In addition, patients with high serum levels of S1P (but not the intermediate metabolites sphinganine and SM) had more advanced-stage, higher-grade (poorly differentiated) tumors and worse overall survival and relapse-free survival (Fig. 1, K and L, and fig. S1, D and E).

We reasoned that high S1P levels may affect a tumor immune microenvironment. Analysis of tumor-infiltrated immune cells by flow cytometry showed that S1P levels in tumor tissues had substantially positive correlations with the numbers of major immunosuppressive cells in HCC, including $CD206^+$ TAMs ($P = 0.009$, $R = 0.2533$) and T_{regs} ($P = 0.004$, $R = 0.2868$), but had negative correlation with the effector $CD8^+$ T cells (Fig. 1M). Consistently, no substantial correlations were seen between the levels of intermediate metabolites (C16 sphinganine and SM) and the numbers of tumor-infiltrated immune cells (fig. S1F).

In both orthotopic (orthotopic injection of Hep-53.4 cells into C57BL/6 mouse) and immunocompetent HTVi mouse HCC models, we further assessed the impact of S1P metabolism on HCC tumor growth and the tumor immune microenvironment in vivo. To this end, tumor-bearing mice in the two mouse models were treated with S1P (20 mg/kg, intraperitoneal injection once every 2 days). We observed that treatment of S1P profoundly promoted HCC tumor growth and consequently decreased mouse survival in both tumor models (Fig. 1, N and O), along with the elevated immunosuppressive TME (increased numbers of $CD163^+$ $F4/80^+$ macrophages and T_{regs} and decreased numbers of $CD8^+$ T cells and T_H17 cells; Fig. 1, P and Q). By contrast, these effects of S1P treatment were not observed in HTVi tumor models using immunodeficient NU/J nude mice (Fig. 1, R and S), indicating that S1P promotes HCC tumor progression via immune regulation.

Collectively, these data demonstrated that S1P metabolism was substantially up-regulated in immunotherapy-resistant HCC tumors. S1P levels in tumors are correlated with immunosuppressive TME and increased levels of S1P in vivo promoted HCC tumor growth in an immune-dependent manner, indicating its potential as a clinical indicator for HCC prognosis and immunotherapy response.

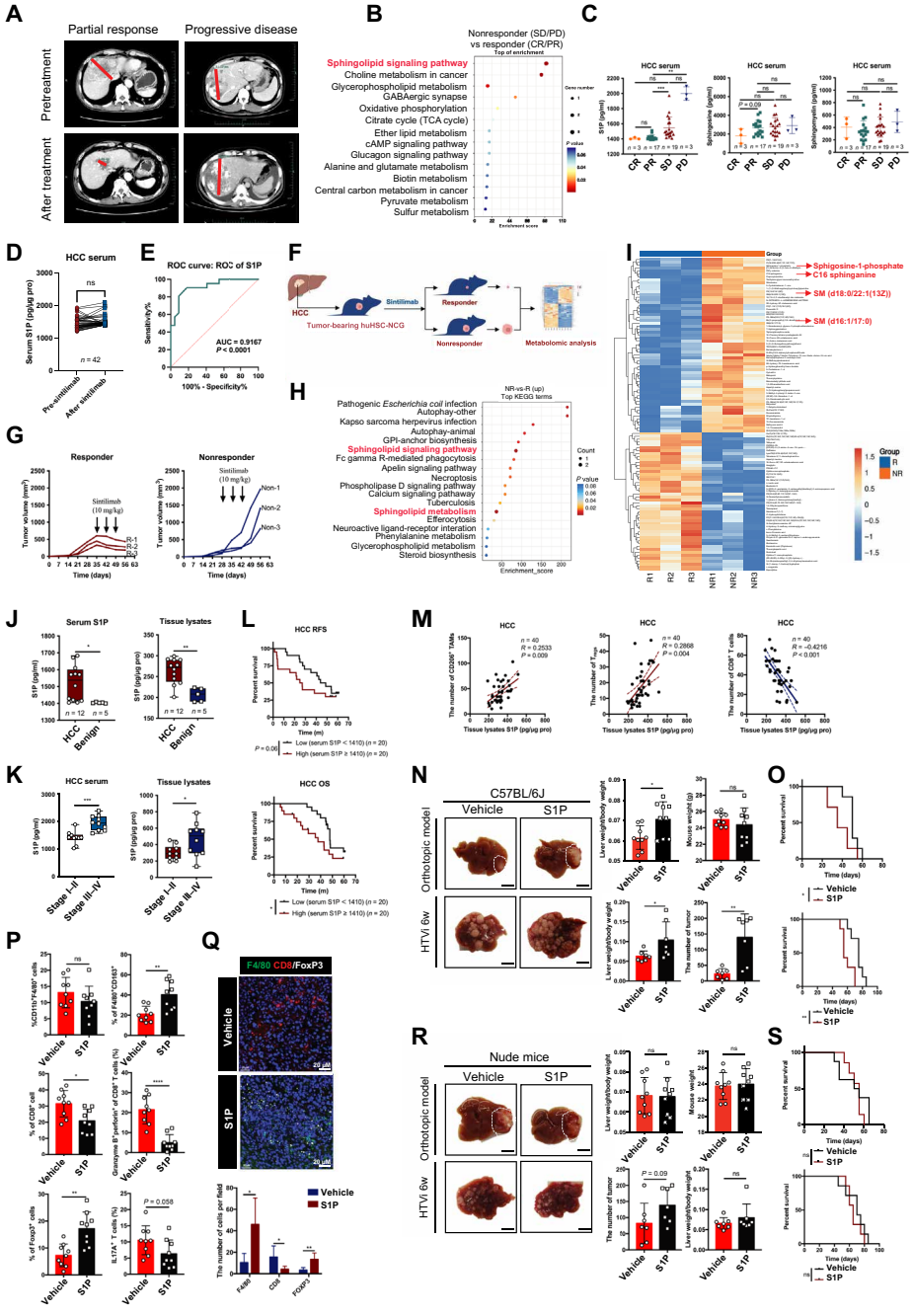

Fig. 1. S1P metabolism is elevated in the αPD-1 resistance group and contributes to HCC progression in an immune-dependent manner. (**A**) Represent images of responder (PR) and nonresponder (PD) in a clinical trial. (**B**) KEGG by LC-MS metabonomics of serum in the responder group ($n = 20$)/nonresponder group ($n = 10$). TCA, tricarboxylic acid; cAMP, cyclic adenosine 3′,5′-monophosphate. (**C**) S1P, sphinganine, and SM levels in serum from patients with CR, PR, SD, and PD treated with sintilimab. (**D**) S1P level in serum from patients before and after sintilimab treatment. (**E**) ROC evaluating of S1P as a predictive biomarker for immunotherapy response. AUC, area under the curve. (**F**) Schematic of model establishment, sample collection, and analysis. (**G**) Tumor volume changes in huHSC-NCG mice treated with sintilimab (responder versus nonresponder). (**H** and **I**) KEGG and heatmap analysis of tumor tissues in responder (R)/nonresponder (NR) groups by LC-MS metabonomics. GPI, glycosylphosphatidylinositol; PE, phosphatidylethanolamine; PI, phosphatidylinositol; PA, phosphatidic acid; PS, phosphatidylserine; PC, phosphatidylcholine; PG, phosphatidylglycerol. (**J** and **K**) S1P level in serum and tissue lysates from HCC, benign, stage I to II, and stage III to IV patients. (**L**) Relapse-free survival (RFS) and overall survival (OS) of patients with HCC between low and high serum S1P. (**M**) Correlation of $CD206^+$ TAMs, $FOXP3^+$ T_{regs}, $CD8^+$ T cells, and tissue S1P levels in HCC. (**N** and **O**) Representative images, statistics, and survival curve of immunocompetent mice treated with vehicle/S1P in orthotopic and HTVi models. (**P**) Flow cytometry of tumor tissues in orthotopic model (vehicle versus S1P). (**Q**) Immunofluorescence of tumor tissues in HTVi model (vehicle versus S1P). (**R** and **S**) Representative images, statistics, and survival curve of immunodeficient mice treated with vehicle/S1P in orthotopic/HTVi model. $^*P < 0.05$, $^{**}P < 0.01$, and $^{****}P < 0.0001$. ns, not significant. Using a two-tailed, unpaired Student's *t* test [(I), (J), (M), (O), (P), and (Q)], nonparametric test, post hoc comparison is Dunn's test [S1P in (C)], one-way analysis of variance (ANOVA) test post hoc comparison is Tukey test [sphinganine/SM in (C)], Pearson correlation test (L), or log-rank test [(K), (N), and (R)]. Data are from ≥3 independent experiments (means ± SD).

S1P induces an immunosuppressive TME

As shown in Fig. 1 (O and P), in vivo treatment with S1P increased the numbers of immunosuppressive TAMs (M2 type) and T_{regs} and reduced the numbers of $CD8^+$ effector T cells and T_H17 cells in HCC tumors. This was also accompanied by reduced activity of $CD8^+$ T cells, indicated by lower levels of cytotoxic molecule granzyme B (GZMB) expression. Given the dynamic nature of TAMs, we wanted to examine the effect of S1P on the isolated TAMs in vitro. S1P treatment promoted the switch of TAMs to M2 type (Fig. 2, A and B, and fig. S2A) and induced the expression of immune checkpoint protein programmed cell death 1 ligand 1 (PD-L1) in TAMs (fig. S2B). Previous studies have reported that lipid metabolites support mitochondrial energy metabolism, governing macrophage polarization, function of $CD8^+$ T cells, and phenotype of T_{regs} (*16*–*19*). Therefore, we hypothesized that S1P may be involved in regulation of mitochondrial respiration in TAMs. To this end, we performed MitoTracker green staining, transmission electron microscopy (TEM), adenosine triphosphate (ATP) production, and Seahorse assays to evaluate the number and function of mitochondria in TAMs. The results showed that S1P-treated TAMs exhibited higher numbers of mitochondria (Fig. 2, C and D), greater mitochondrial oxidative phosphorylation (OXPHOS) for enhanced ATP synthesis, but not glycolysis (Fig. 2, E and F). We further discovered that mitochondrial synthesis inhibitors can reverse S1P-induced M2 polarization of macrophages, suggesting that S1P-induced M2 polarization of macrophages is likely mediated through mitochondrial synthesis (fig. S2C).

We next tested whether the addition of S1P could remodel the function and metabolism of other types of immune cells. Consistent with in vivo results, S1P directly suppressed the proliferation and cytotoxicity of $CD8^+$ T cells and induced their exhaustion (Fig. 2, G to J, and fig. S2A). In addition, the treatment of S1P skewed the differentiation of $CD4^+$ T cells to $FOXP3^+$ T_{regs} but suppressed their differentiation to T_H17 cells, thereby enhancing immunosuppressive capability as shown by flow cytometric analysis and immunosuppressive assays (Fig. 2, K to M, and fig. S2A). Similarly, we investigated the roles of S1P in cell metabolism of $CD8^+$ T cells and T_{regs}. In contrast to what are observed in TAMs, S1P decreased the number of mitochondria, ATP production, oxygen consumption rate (OCR), and extracellular acidification rate (ECAR) in $CD8^+$ T cells (Fig. 2, N to P), indicating that both glycolysis and mitochondrial OXPHOS were suppressed. This is consistent with the exhausted state of $CD8^+$ T cells after S1P treatment. However, S1P increased the number of mitochondria, ATP production, and maximal OCR in T_{regs} (Fig. 2, Q to S), as in TAMs. Before S1P stimulation, we pretreated TAMs and $CD4^+$ T cells with mitochondrial respiratory chain inhibitors (rotenone) and mitochondrial RNA polymerase (POLRMT) allosteric inhibitors (IMT1B), In contrast, $CD8^+$ T cells were treated with enhancement of mitochondrial biosynthesis (mitochondrial fusion promoter M1). Our study demonstrates that mitochondrial synthesis inhibitors could reverse S1P-induced M2 conversion and Foxp3 differentiation, while enhancing mitochondrial biogenesis (mitochondrial fusion promoter M1) prevents the development of T cell exhaustion in S1P-treated population (fig. S2, C to E).

To explore mechanism by which S1P regulates the differentiation of $CD4^+$ T cells to $Foxp3^+$ T_{regs}, we performed the phosphoproteomic analysis by LC-MS and found that phosphatidylinositol-4,5-bisphosphate 3-kinase (PI3K)-protein kinase B (Akt)-mammalian target of rapamycin (mTOR) signaling pathway was activated in $CD4^+$ T cells after S1P treatment (fig. S2F), as previous studies reported (*20*, *21*). Western blotting assay confirmed that p-PI3K, p-Akt, p-mTOR, and FOXP3 levels were up-regulated after S1P treatment (fig. S2G). We pretreated $CD4^+$ T cells with LY294002 (PI3K inhibitor), MK-2206 2HCl (Akt inhibitor), and rapamycin (mTOR inhibitor), respectively, and cocultured with TAMs. As we expected, the expression of FOXP3 and the activation of PI3K-Akt-mTOR signaling pathway were rescued by these inhibitors (fig. S2H), indicating that S1P promotes the expression of Foxp3 by activating the PI3K/Akt/mTOR pathway. Consistent with mechanisms observed in T_{regs}, the activation of PI3K-Akt-mTOR signaling pathway was observed and involved the switch of TAMs to M2 type mediated by S1P (fig. S2, I and J).

These results demonstrate that S1P directly induces mitochondrial metabolism and the immunosuppressive phenotype of TAMs and T_{regs} while reducing proliferation and energy metabolism and promoting exhaustion in $CD8^+$ T cells. This suggests that S1P metabolism contributes to immunosuppressive TME via immunometabolic reprogramming.

TAMs is a main source of S1P in TME

The metabolic pathway for biosynthesis of sphinganine, SM, and S1P involves a number of enzymes, including SPT, 3-ketosphinganine reductase, ceramide synthase, dihydroceramide desaturase, and SM synthase (Fig. 3A). SPT locates in the ER membranes and is the rate-limiting enzyme in this pathway (*22*). To determine what types of cells are the primary sources to produce S1P, we assessed the enzymatic activity of SPT using a specific enzymatic activity assay (*23*). We found that SPT activity in TAMs is remarkably higher than in tumor cells, hepatic stellate cells (HSCs), as well as other types of immune cells (Fig. 3B). In line with high enzymatic activity of SPT in TAMs, S1P levels in the cell culture medium of TAMs are also extremely high (Fig. 3C), suggesting that TAMs are a main source for secreted S1P in the TME.

To further investigate whether S1P derived from TAMs contributes to immunosuppressive TME, we tested whether inhibiting the S1P signaling could mitigate the immunosuppressive effects of TAMs. We observed that pretreatment of S1P antagonist (S1PR antagonist) fingolimod rescued the proliferation, glycolysis, and tumor cell killing capacity of $CD8^+$ T cells when cocultured with TAMs (fig. S3, A to D). As expected, the fingolimod almost completely offsets the mitochondrial metabolism and immunosuppressive function of T_{regs} induced by TAMs (fig. S3, E to G).

To explore the role of TAMs in ICB resistance and tumor progression, we isolated macrophages from the tumors of the same HCC humanized mouse models treated with sintilimab as in Fig. 1E. We then conducted RNA sequencing (RNA-seq) analysis on TAMs isolated from those responders and nonresponders (Fig. 3D). Analysis of the RNA-seq data showed that the *NEK2* gene is one of the top-ranked genes whose expression increased most substantially in the TAMs from nonresponders compared to those from responders (Fig. 3E). Flow cytometry (Fig. 3F), multiplex immunohistochemistry (mIHC) (Fig. 3G), and Western blotting (Fig. 3H) also confirmed that NEK2 expression was drastically increased in macrophages from tumor tissues compared to the para-tumor control tissues, particularly in the tumor tissues of nonresponders. Consistent with our findings, single-cell RNA-seq (scRNA-seq) analyses of public datasets also validated the presence of $NEK2^{hi}$ TAMs in liver cancer, included in the subpopulation of $STMN1^+$ macrophages (fig. S4, A and B).

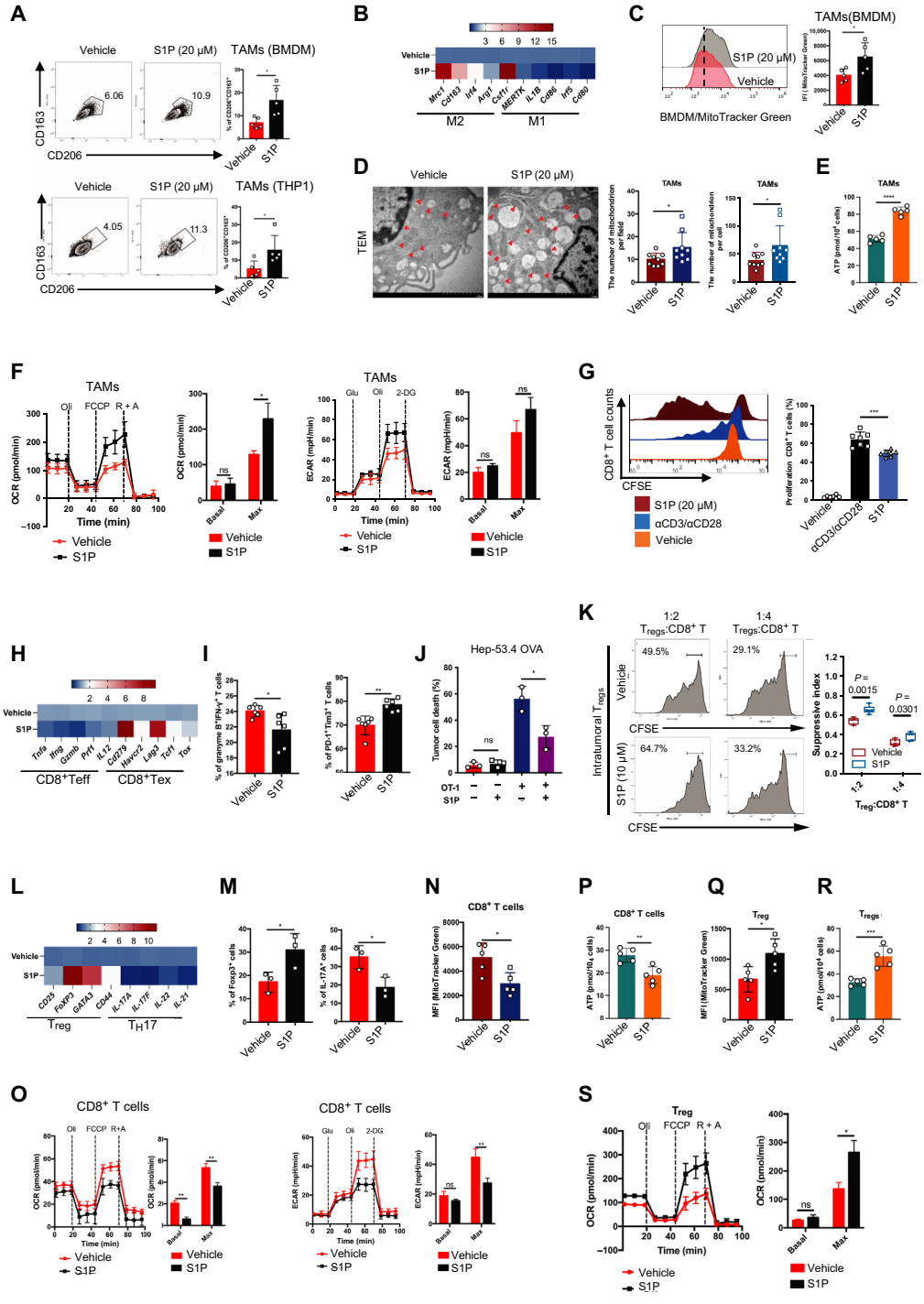

Fig. 2. S1P metabolism mediates an immunosuppressive phenotype and reprograms immunometabolism. (**A**) Flow cytometric analysis of TAMs with vehicle and S1P. (**B**) Expression of genes encoding M2 and M1 phenotype in macrophages with vehicle and S1P (20 μM) by reverse transcription polymerase chain reaction (RT-PCR). (**C**) MitoTracker Green of TAMs with vehicle and S1P (20 μM). (**D**) Representative images and statistical results of mitochondrial (red arrowheads) of TAMs with vehicle and S1P by TEM. (**E** and **F**) ATP determination and Seahorse analysis in TAMs with vehicle and S1P. 2-DG, 2-deoxyglucose. (**G**) Proliferation measured by CFSE in $CD8^+$ T cells with vehicle and S1P (20 μM). (**H**) Expression of genes encoding function of $CD8^+$ T effector cells (Teff) and $CD8^+$ T exhausted cells (Tex) with vehicle and S1P (20 μM) by RT-PCR. (**I**) Statistical results of GZMB and tumor necrosis factor–α (TNFα) in $CD8^+$ T cells with vehicle and S1P (20 μM). (**J**) OT-1 T cell–meditated tumor cell killing assay in Hep-53.4 OVA treated with vehicle and S1P. (**K**) Ex vivo suppression of CFSE-labeled WT naïve $CD8^+$ T cell proliferation by T_{regs} with vehicle and S1P (10 μM). (**L**) Expression of genes encoding function of T_{regs} and T_H17 cells with vehicle and S1P (10 μM) by RT-PCR. (**M**) Statistical results of FoxP3 and IL-17A in $CD4^+$ T with vehicle and S1P. (**N** to **P**) MitoTracker Green, Seahorse analysis and ATP determination of $CD8^+$ T cells with vehicle and S1P (20 μM). (**Q** to **S**) MitoTracker Green, Seahorse analysis, and ATP determination of T_{regs} with vehicle and S1P (10 μM). $^*P < 0.05$, $^{**}P < 0.01$, $^{***}P < 0.001$, and $^{****}P < 0.0001$. Using a two-tailed, unpaired Student's *t* test [(A), (C), (D), (E), (F), (G), (I), (J), (K), and (M) to (S)]. Data are from ≥3 independent experiments (means ± SD).

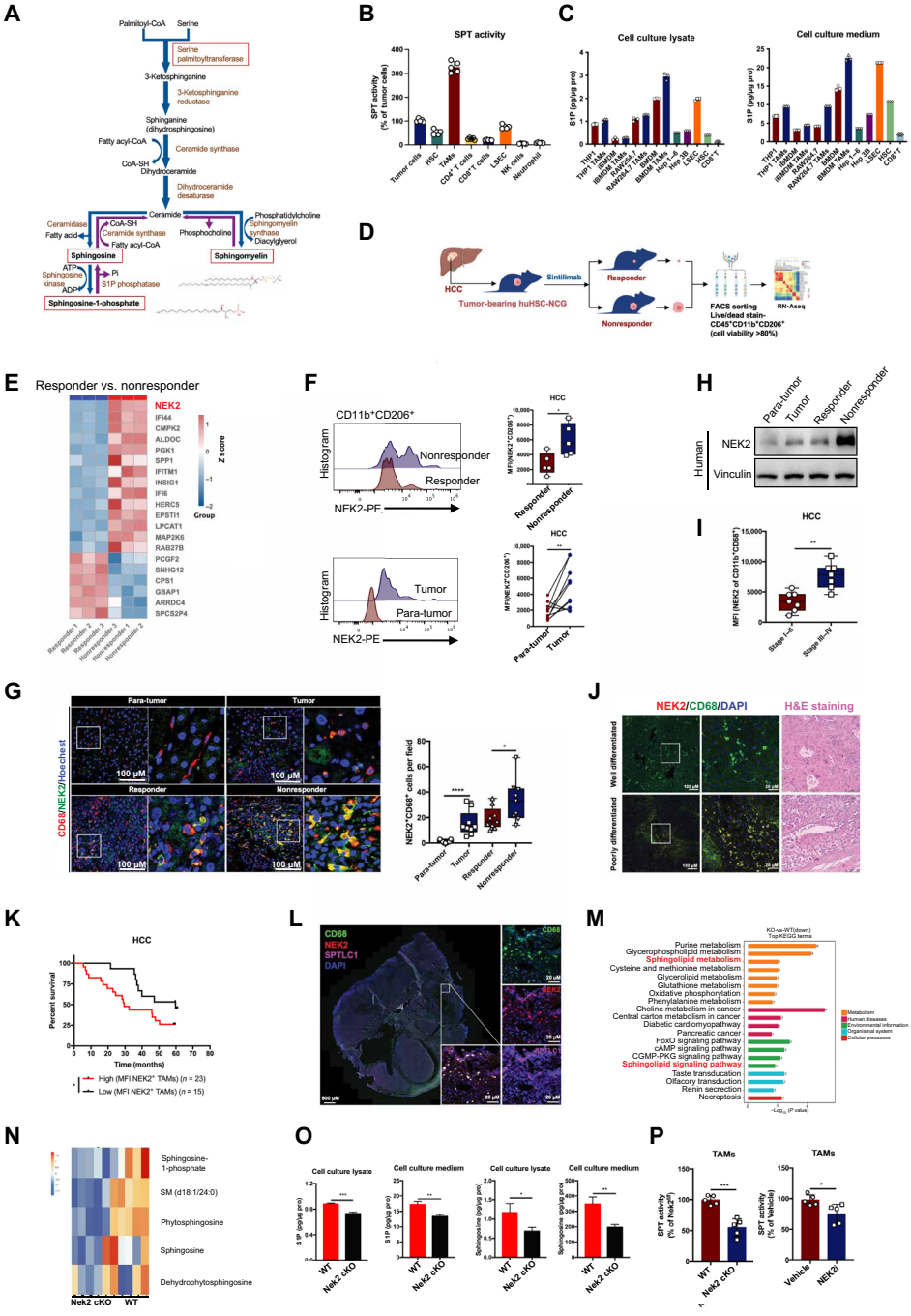

Fig. 3. NEK2^{hi} TAMs, which was the main source of S1P-related metabolites, were identified as a driver for immunotherapy resistance. (**A**) Biochemical pathways for de novo S1P and SM synthesis. ADP, adenosine diphosphate; Pi, inorganic phosphate. (**B**) SPTLC activity of tumor cell and immune cell sorting from HCC tissues ($n = 5$). (**C**) Concentration analysis of S1P by ELISA in cell culture lysates and medium of indicated cells. (**D**) Schematic diagram showing the process of model establishment, sample collection, and analysis. (**E**) RNA-seq analysis of HCC-associated TAMs in responder and nonresponder groups. (**F**) Representative histograms further quantification of NEK2 in TAMs isolated from para-tumor, tumor, responder, and nonresponder samples ($n = 5$). (**G**) Representative images and statistical results showing immunofluorescence staining of indicated antibodies in para-tumor, tumor, responder, and nonresponder sample ($n = 9$). (**H**) Western blot of NEK2 in TAMs isolated from para-tumor (normal), tumor, responder, and nonresponder samples. (**I**) Mean fluorescence intensity (MFI) analysis of NEK2^{hi} TAMs in tumor tissue from stage I to II ($n = 7$) and stage III to IV patients ($n = 7$). (**J**) Representative images showing immunofluorescence staining of NEK2^{hi} TAMs in well differentiated and poorly differentiated samples. H&E, hematoxylin and eosin. (**K**) Correlation of NEK2 in TAMs with prognostic factors in patients with HCC. (**L**) Multiple IHC labeling using indicated antibodies in tumor tissues. (**M** and **N**) KEGG and heatmap analysis of TAMs by LC-MS metabonomics from WT and *Nek2cKO* mice. CGMP-PKG, cyclic guanosine monophosphate-protein kinase G signaling pathway. (**O**) Concentration analysis of S1P and sphinganine by ELISA in cell culture lysates and medium of TAMs from WT and *Nek2cKO* mice. (**P**) SPTLC activity of TAMs from WT and *Nek2cKO* mice or with a NEK2 inhibitor (10 μM) ($n = 5$). $^*P < 0.05$, $^{**}P < 0.01$, $^{***}P < 0.001$, and $^{****}P < 0.0001$. Using a two-tailed, unpaired Student's *t* test [(F), (G), (I), (O), and (P)] or log-rank test (K). Data are from ≥3 independent experiments (means ± SD). DAPI, 4′,6-diamidino-2-phenylindole.

Given the complexity of cell composition in tumor tissues, we analyzed NEK2 expression in tumor cells and various types of stromal cells, including infiltrated T cells, natural killer (NK) cells, B cells, and cancer-associated fibroblasts by flow cytometry. Five naïve human pancreatic tumor samples were surgically resected and analyzed. It was obvious that NEK2 was mainly expressed in TAMs and tumor cells, compared to all the other types of cells in the TME (fig. S4C). The presence of NEK2^{hi} TAMs was also verified in patient pancreatic tumor samples by mIHC (fig. S4D). NEK2 expression is correlated with the stage and pathological grade of HCC. According to the tumor, node and metastasis stage classification, NEK2 expression was lower in TAMs of grades I to II HCC tumors than in grades III to IV tumors (Fig. 3I). In addition, NEK2^{hi} TAMs were enriched in poorly differentiated tumors (Fig. 3J). Moreover, high NEK2 expression in TAMs was associated with worse prognosis in patients with HCC (Fig. 3K), suggesting that NEK2 expression in TAMs is associated with HCC tumor progression and therapeutic resistance.

mIHC staining of human HCC tumor tissues confirmed that NEK2 was nicely coexpressed with SPTLC1 (an SPT isoform) in TAMs (Fig. 3L). Given the correlation of S1P metabolism and NEK2 in TAMs, we reasoned that NEK2 may act as a direct or indirect regulator in the S1P-related metabolism in TAMs. To test this hypothesis, we first conducted MS-based metabolite profiling of wild-type (WT) and *Nek2*–knockout (KO) mouse TAMs. Substantial changes in the sphingolipid metabolism pathway were seen using KEGG enrichment analysis. The levels of S1P were substantially lower in the *Nek2-KO* TAMs compared to WT TAMs (Fig. 3, M and N). NEK2 depletion also reduced the secretion of S1P and related metabolites from TAMs, as shown by a S1P ELISA assay (Fig. 3O and fig. S4E). In addition, the analysis of S1P levels in tumor tissue lysates and serum from both WT and *Nek2cKO* mice yielded similar results (fig. S4G). Similarly, inhibition of NEK2 by a small molecule inhibitor also decreased the production of S1P and related metabolites (fig. S4F). The enzymatic activity of SPT had a marked decline in *Nek2-KO* or NEK2-inhibited TAMs (Fig. 3P). Together, these data indicate that NEK2^{hi} TAMs are the main source of S1P in HCC tumors.

NEK2 phosphorylates SPTLC1 at S401 to promote the activity of SPT

As the rate-limiting enzyme in the S1P biosynthesis pathway, SPT is a holocomplex consisting of catalytic components (SPTLC1 and SPTLC2) and regulatory components [serine palmitoyltransferase small subunit A (ssSPTa) and ORMDL sphingolipid biosynthesis regulator 3 (ORMDL3)] in *Homo sapiens* and *Mus musculus* (*24*). While ssSPTa is a positive regulator that determines substrate selectivity and enhances the SPT activity, ORMDL3 functions as a negative regulator that reduces the SPT activity (*25*). We hypothesized that NEK2 reprograms S1P metabolism by direct or indirect interaction with the SPT complex. Molecular docking was conducted to gain mechanistic insight into their interaction. The result of in silico analysis revealed that NEK2 binds to the SPT complex and docks at the ORMDL3 position (Fig. 4A), indicating that NEK2 may inhibit the negative regulation of ORMDL3 through competitive occupancy, thereby promoting SPT activity. We also observed that SPTLC1 has greater binding to ORMDL3 in NEK2-KO BMDMs. Notably, there was no substantial change in SPTLC1 expression in the absence of NEK2, indicating that NEK2 may regulate SPTLC1-containing SPT activity rather than SPTLC1 expression (Fig. 4B).

To determine which SPT isoform directly interacts with NEK2, each of the SPT components with hemagglutinin tag and FLAG-tagged NEK2 was coexpressed in human 293T cells, and coimmunoprecipitation (IP)–Western blotting assays was conducted to examine their physical interactions. The results showed that NEK2 binds SPTLC1 specifically but only weakly with other SPT components, indicating that SPTLC1 is likely a direct interactor of NEK2 (Fig. 4C). Reciprocal IP–Western blotting analysis confirmed the NEK2-SPTLC1 interaction in TAMs from mouse bone marrow–derived macrophages (BMDMs) (Fig. 4D). In addition, a GST (glutathione *S*-transferase) affinity assay validated the direct interaction of SPTLC1-GST with NEK2-His (Fig. 4E). The binding affinity of NEK2 to SPTLC1 protein was measured by microscale thermophoresis (MST) assay with a dissociation constant (K_d) of ~350 nM, indicating relatively strong protein-protein interaction in vitro (Fig. 4F). A Duo-link assay demonstrated their real intracellular interaction (Duo: red) at the ER (HSP90B1: green) in TAMs (Fig. 4G). To determine where the NEK2-SPTLC1 interaction takes place, Triton X-100 was used to disrupt the ER membrane of BMDMs. In the samples without added Triton X-100, the protein marker HSP90B1 inside the ER lumen and NEK2 remained largely unchanged, while the extraluminal marker inositol-requiring enzyme 1α (IRE1α) degraded rapidly. In the samples with Triton X-100 permeabilization, both luminal and extraluminal proteins degraded rapidly (Fig. 4H). This experiment demonstrates that NEK2 mainly localizes inside the ER lumen for its function.

Given that NEK2 is a protein kinase, we wanted to examine whether SPTLC1 is a substrate of NEK2. Phosphoproteomic analysis by LC-MS revealed that NEK2 overexpression boosted the phosphorylation level of SPTLC1 at the S50/S381/S401/S404 residues (Fig. 4I and table S3). To determine which site(s) mediates NEK2 regulation of SPTLC1, we geneated four constitutively nonphosphorylated mutants of SPTLC1 (S50A, S381A, S401A, and S404A). Protein interaction analyses showed that the S401A mutation abolishes the interaction of NEK2 with SPTLC1 (Fig. 4J). The results from Duo-link assay also supported that S401 phosphorylation may be essential for the NEK2-SPTLC1 interaction (Fig. 4K). A specific antibody was generated for phosphorylated SPTLC1 at S401. A notable reduction of the S401 phosphorylation levels of SPTLC1 was observed in the presence of a NEK2 inhibitor or in NEK2-KO TAMs (Fig. 4L). In vitro kinase assay demonstrated that NEK2 directly phosphorylates SPTLC1 at the S401 residue (Fig. 4M).

Together, our results support the hypothesis that NEK2 enhances SPT complex enzymatic activity by competitively occupying the negative regulator ORMDL3 and positively regulate SPTLC1 via S401 phosphorylation inside the ER lumen.

NEK2 in macrophages drives tumorigenesis in an immune-dependent manner

To study the physiological effect of NEK2 in macrophages, we generated myeloid-specific conditional KO mice deficient in NEK2 by crossing *Nek2f/f* with *Lyz2Cre* mice (*Nek2f/f* × *Lyz2Cre*; designated *Nek2cKO*) [genotype identification and phenotype validation are shown in fig. S5 (A and B)]. Tissue microenvironment remodeling in liver is crucial for tumor initiation and progression. To investigate the impact of Nek2 deletion in macrophages on the remodeling of the liver immune microenvironment, we performed scRNA-seq of freshly dissociated liver samples from WT and *Nek2cKO* mice. We charted the landscape of tumor immune microenvironment before

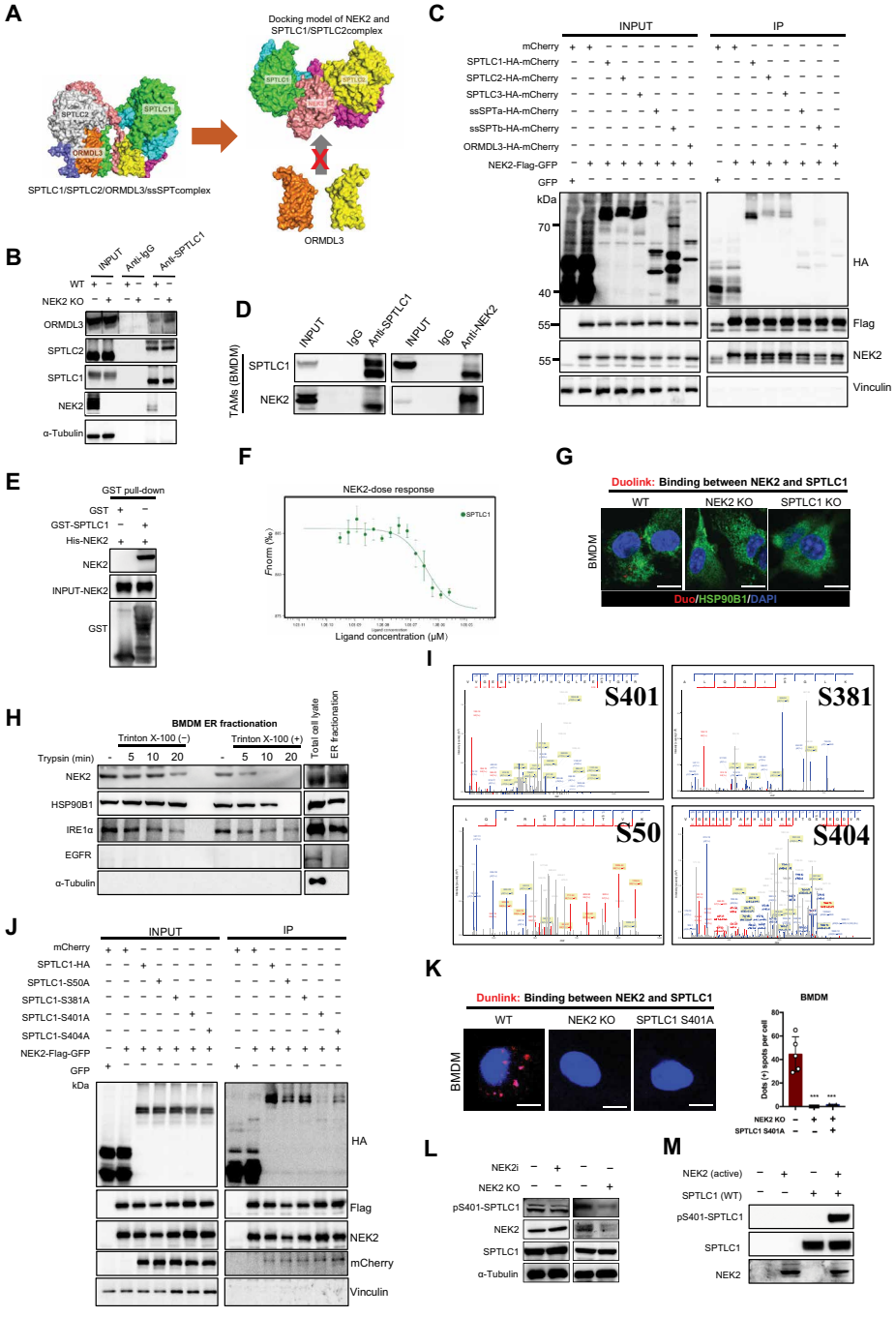

Fig. 4. NEK2 phosphorylates SPTLC1 at S401 to promote kinase metabolic activity. (**A**) Docking model of NEK2 (2XNM) and SPTLC1/SPTLC2 complex (7K0M). (**B**) Cell lysates from BMDMs analyzed by immunoprecipitation (IP) and Western blot using the antibodies indicated. (**C**) Western blot analysis of whole-cell lysates and anti-Flag IP derived from 293T cells transfected with indicated constructs. Cells were treated with 10 μM MG132 for 12 hours before harvesting. (**D**) IP and Western blot using the antibodies indicated in cell lysates from BMDMs. Representative images are shown. (**E**) GST pull-down assay of NEK2-His and GST-SPTLC1 protein. Representative images are shown. $n = 3$ independent experiments. (**F**) Microscale thermophoresis (MST) analysis of NEK2-SPTLC1 interaction measurements. (**G**) Representative images of individual immunofluorescence staining of NEK2 and SPTLC1 interaction in BMDM cells by Duolink assay combined with immunofluorescence staining using markers for ER (HSP90B1) and nuclei (DAPI). The red dots (NEK2/PD-L1 interaction) indicate their interaction. (**H**) Trypsin digestion of ER fractions with or without permeabilization in BMDM cells. Representative image is shown, $n = 3$ independent experiments. (**I**) SPTLC1 phosphorylation at the S401/S381/S404/S50 residues were identified by MS analysis. (**J**) Immunoblotting (IB) analysis of Input and anti-Flag IP derived from 293T cells transfected with indicated constructs. Cells were treated with 10 μM MG132 for 12 hours before harvesting. (**K**) Representative images and statistical results of individual immunofluorescence staining of the NEK2 and SPTLC1 interaction in BMDM cells by a Duolink assay. The red dots (NEK2/SPTLC1 interaction) indicate their interaction. (**L**) IB analysis of S401-phosphorylated SPTLC1 in BMDM cells with NEK2 inhibitor (10 μM, 48 hours) and NEK2 KO BMDM. (**M**) In vitro kinase assay and IB analysis of pS401-SPTLC1 expression of recombinant SPTLC1 WT and NEK2 (active) protein. Representative images are shown. $n = 3$ independent experiments. IgG, immunoglobulin G; GFP, green fluorescent protein; HA, hemagglutinin; *m/z*, mass/charge ratio.

hepato-carcinogenesis with UMAP plots. A list of differentially expressed genes (DEGs) that defined the clusters is presented in table S4. Upon analysis of the DEGs, we identified 14 major cell types, including B cells, $CD4^+$ T cells, $CD8^+$ T cells, conventional dendritic cells, endothelial cells, fibroblasts, granulocytes, hepatocytes, macrophages, monocytes, NK cells, natural killer T (NKT) cells, plasmacytoid dendritic cells, and T_{regs} (fig.S5C). By comparing dynamic changes in $CD45^+$ cells (fig. S5D, left) and live cells (fig. S5D, right) of dissociated liver cells between WT and *Nek2cKO* mice, we found marked increases in NK, NKT cells, and liver sinusoidal endothelial cells in *Nek2cKO* mice. Flow cytometrical analyses confirmed these changes (fig. S5E). KEGG pathway analysis also showed that the OXPHOS pathway was globally up-regulated in almost all the immune cells in *Nek2cKO* livers (fig. S5F), suggesting that NEK2 in macrophages may remodel the preneoplastic immunometabolism in the liver.

Next, we used an HTVi-induced HCC mouse model (NRas V12/c-Myc, see details in Materials and Methods) to examine the role of NEK2 in macrophages in hepatocarcinogenesis. KO of Nek2 in macrophages resulted in postponed tumor occurrence and a reduced incidence of liver tumors, compared with WT control mice (Nek2f/f) (Fig. 5A). The ratio of liver weight to body weight was markedly smaller, and the number of tumors in the HTVi model was profoundly reduced in the *Nek2cKO* mice due to reduced tumorigenesis (Fig. 5B). Additional flow cytometric analysis revealed that the tumors in *Nek2cKO* mice had a diminished number and M2-like TAMs, a shift from T_{regs} to a more T_H17-like phenotype, and increased function of $CD8^+$ T cells (fig. S6, A and B). Immunofluorescence staining confirmed these results (Fig. 5C). Notably, the depletion of NEK2 in macrophages prolonged survival in animal models (Fig. 5D).

To determine whether $NEK2^{hi}$ macrophages drive hepatocarcinogenesis in an immune-dependent manner, we established HTVi liver tumor models in immunocompetent C57BL/6J mice and immunodeficient Nu/J mice whose macrophages were predepleted with clodronate liposomes (*26*). Mono-macrophages (2×10^6 each mouse) isolated from WT or *Nek2cKO* mice were subsequently transferred to the macrophage-cleared mice via intravenous injection (tail vein intravenously) (fig. S6C) (details in Materials and Methods). In comparison with the WT macrophage group, the number of liver tumors and relative liver weight in the Nek2-KO macrophage group were both remarkably reduced in the immunocompetent mice but not in the immunodeficient nude mice (fig. S6, D and E). As a result, the tumor-bearing immunocompetent mice with *Nek2cKO* macrophages had extended survival, which was not observed in the immunodeficient mice (fig. S6F). Macrophages in HCC consist of Kupffer cells and monocyte-derived macrophages (*27*). No substantial differences were observed in tumor numbers, relative liver weight, and tumor-infiltrating immune cells in HTVi mouse models using WT control (Nek2f/f) or *Nek2f/f* × *Clec4fcre* (Nek2 depletion in Kupffer cells) mice (fig. S7, A to D), indicating that NEK2 signaling pathway in myeloid-derived macrophages, but not in Kupffer cells, is involved in hepatic tumorigenesis. Collectively, these results suggest that NEK2 in macrophages drives HCC tumorigenesis through S1P-meidated immunometabolic reprogramming in the TME in an immune-dependent manner.

NEK2 expression is essential for immunosuppressive functions of TAMs

We next sought to determine how $NEK2^{hi}$ TAMs exert their immunosuppressive functions in TME. As mentioned above, the proportion of M2-like $CD206^+$ TAMs decreased after the deletion of NEK2 in vivo (fig. S6, A and B). Immune profiling analyses of $NEK2^{hi}$ and $NEK2^{low}$ TAMs in patient samples and HTVi mouse model tumor tissues demonstrated a positive correlation between NEK2 level in tumor macrophages and levels of the M2 macrophage markers (CD206, CD163, PD-L2, and RELMα) (Fig. 5E), suggesting that NEK2 may be required for immunosuppressive M2 phenotype. We also observed that NEK2 depletion or inhibition in macrophages, upon stimulation with Hep-53.4 conditioned medium, substantially hindered M2 polarization in vitro (fig. S8, A and B). In addition, we found that NEK2 supports the proliferative capacity of macrophages, as Ki67 expression was greatly inhibited in NEK2-depleted/inhibited macrophages (fig. S8C). We found that NEK2 positively regulated the expression of PD-L1 in TAMs (fig. S8D), similar to its effect in pancreatic tumor cells (*28*).

To further examine the correlation between $NEK2^{hi}$ TAMs and immune cells in TME, we performed mIHC on human HCC tissues ($n = 30$). The results revealed that $NEK2^{hi}$ TAMs negatively correlate with $CD8^+$ T cells but positively correlate with T_{regs} (Fig. 5F). Notably, the number of T_{regs} increased in $NEK2^{hi}$ TAM-enriched areas, while $CD8^+$ T cell infiltration decreased in these areas (Fig. 5G). To confirm the effect of NEK2 in TAMs on $CD8^+$ T cells and T_{regs}, we first performed carboxyfluorescein diacetate succinimidyl ester (CFSE) assay to evaluate the proliferation of $CD8^+$ T cells cocultured with *Nek2 cKO* TAMs. We found that NEK2-depleted or NEK2-inhibited M2 macrophages were less capable of suppressing T cell proliferation (Fig. 5H and fig. S8E). Analysis of T cell function genes (Fig. 5I), T cell activity markers (Fig. 5J), and T cell cytotoxicity (Fig. 5K) in $CD8^+$ T cells cocultured with WT or *Nek2cKO* TAMs indicated that NEK2 expression in TAMs impaired the effector function of $CD8^+$ T cells and that loss of NEK2 in TAMs can confer greater antitumor immunity. Next, we performed gene expression analysis and flow cytometrical analysis in $CD4^+$ T cells cocultured with control or *Nek2cKO* TAMs. We found that $NEK2^{hi}$ TAMs promote FoxP3 expression and decrease IL-17A expression in $CD4^+$ T cells (Fig. 5, L and M). To verify that T_{regs} induced by $NEK2^{hi}$ TAMs can suppress effector T cells, we performed in vitro suppression assay. The results revealed that T_{regs} cocultured with *Nek2cKO* TAMs had decreased suppressive capability compared with T_{regs} cocultured with control TAMs (Fig. 5N). These results were confirmed using NEK2 inhibitor–treated TAMs (fig. S8, F to I).

Metabolic reprogramming has been thought to modulate the functions of immune cells (*29*). We asked whether NEK2 affects cell metabolism in TAMs. As shown by LC-MS energy analysis, NEK2 depletion in TAMs affects multiple energy metabolic pathways (Fig. 5O). Mitochondria are the major energy-generating source for cells. Using flow cytometry and TEM, we found that *Nek2cKO* TAMs displayed an overall lower number of mitochondria compared with WT TAMs (Fig. 5, P and Q, and fig. S9A). This scenario was recapitulated by a NEK2 inhibitor (fig. S9B). We then used the Seahorse assay to assess mitochondrial respiration and oxygen consumption in TAMs isolated from the HTVi mouse HCC model. *Nek2cKO* TAMs or WT TAMs treated with a NEK2 inhibitor showed reduced basal and maximal OCRs and overall ATP production but no substantial difference in glycolytic metabolism (indicated by ECAR) (Fig. 5R and fig. S9, C to E). Similarly, $CD8^+$ T cells cocultured with *Nek2cKO* TAMs had a higher number of mitochondria and enhanced ECAR compared with $CD8^+$ T cells cocultured with WT TAMs (Fig. 5S). However, T_{regs} cocultured with *Nek2cKO* TAMs showed a

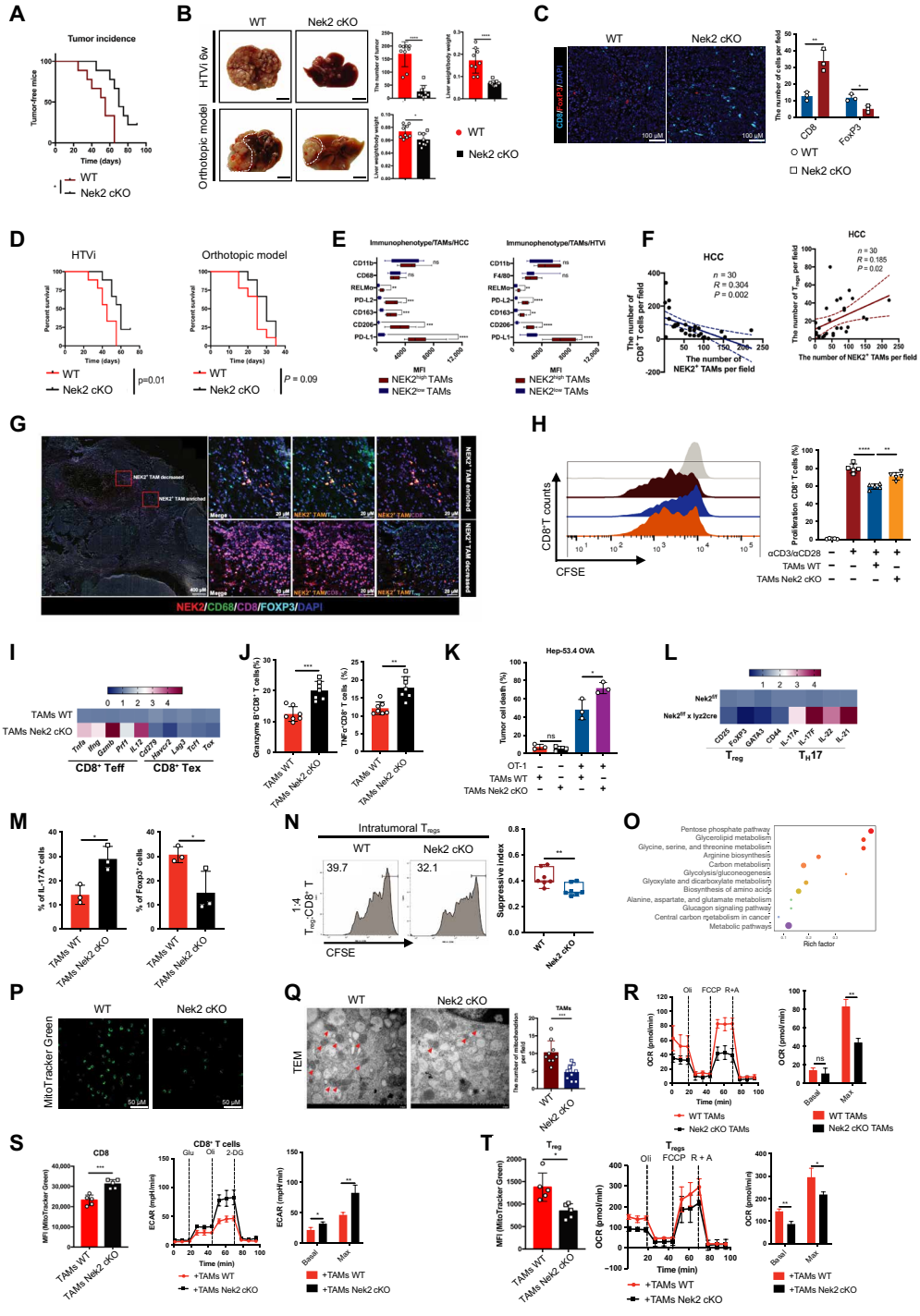

Fig. 5. NEK2 in macrophages drives hepatocarcinogenesis and progress. (**A**) Tumor incidence in WT and *Nek2cKO* mice ($n = 9$). (**B**) Representative images and statistical results of tumor in WT/*Nek2cKO* mice by orthotopic and HTVi model. (**C**) mIHC analysis of $CD8^+$ T cells and $Foxp3^+$ T_{regs} in WT and *Nek2cKO* mice tumors. (**D**) Survival of WT and *Nek2cKO* mice in HTVi and orthotopic model. (**E**) Immunophenotype analysis of $NEK2^{hi}$ TAMs and $NEK2^{low}$ TAMs in patients' HCC and HTVi mice. (**F**) Correlation of $NEK2^{hi}$ TAMs with $CD8^+$ T cells or T_{regs} in a tissue microarray. (**G**) mIHC spatial staining of $NEK2^{hi}$ TAMs, $CD8^+$ T cells, and $FOXP3^+$ T_{regs} in patients' HCC tumors. (**H**) CFSE-based proliferation of $CD8^+$ T cells cocultured with WT/*Nek2cKO* TAMs. (**I** and **J**) RT-PCR analysis of $CD8^+$ Teff/Tex and GZMB and TNFα expression in $CD8^+$ T cells cocultured with WT/*Nek2cKO* TAMs. (**K**) OT-1 T cell–meditated killing of Hep-53.4 OVA with WT/*Nek2cKO* TAMs. (**L** and **M**) RT-PCR analysis of T_{regs} and T_H17 cells and flow cytometric analysis of Foxp3/IL-17A in T_{regs} cocultured with WT/*Nek2cKO* TAMs. (**N**) Ex vivo suppression of CFSE-labeled WT naïve $CD8^+$ T cell proliferation by T_{regs} cocultured with WT/*Nek2cKO* TAMs. (**O**) KEGG analysis by LC-MS energy reanalysis of WT/*Nek2cKO* TAMs. (**P**) MitoTracker Green of WT/*Nek2cKO* TAMs. (**Q**) TEM analysis of mitochondrial (red arrowheads) from WT and *Nek2cKO* TAMs. (**R**) Representative OCR of WT and *Nek2cKO* TAMs. (**S** and **T**) MitoTracker Green and Seahorse analysis of $CD8^+$ T cells and T_{regs} cocultured with WT/*Nek2cKO* TAMs. $^*P < 0.05$, $^{**}P < 0.01$, $^{***}P < 0.001$, and $^{****}P < 0.0001$. Using a two-tailed, unpaired Student's *t* test [(B), (C), (H), (J), (K), (M), (N), (Q), (R), (S), and (T)], Pearson correlation test (F), or log-rank test [(A) and (D)]. Data are from ≥3 independent experiments (means ± SD).

lower number of mitochondria and decreased OCR compared with $CD8^+$ T cells cocultured with WT TAMs (Fig. 5T). As expected, NEK2 inhibition had a similar effect as NEK2 KO (fig. S9, F to I). Last, the findings demonstrated that *Nek2cKO* leads to decreased mitochondrial numbers and reduced lipid metabolism levels in both TAMs and T_{regs}, while increasing mitochondrial numbers in $CD8^+$ T cells were also validated in in vivo models (fig. S9, J and K). The levels of S1P in serum and tissue lysates were substantially lower in the *Nek2cKO* model compared to WT, consistent with our in vitro observations shown in Fig. 3O (fig. S9L). Collectively, these findings suggest that NEK2 activation in macrophages promotes an immunosuppressive M2 phenotype through energy metabolic reprogramming and that suppression of NEK2 signaling not only inhibits the immunosuppressive activity but also disrupts mitochondrial energy metabolism.

Depletion of NEK2 in TAMs sensitizes PD-1–based immunotherapy

Given that NEK2 inhibition in TAMs can alleviate immunosuppressive TME, a critical question is whether reinvigorating exhausted T cells with PD-1 blockade can synergize with NEK2 inhibition in TAMs for immunotherapy against HCC. To address it, we investigated the effect of NEK2 depletion in TAMs on enhancing the efficacy of ICB therapy in HCC. HCC tumor models were established by orthotopic injection of Hep-53.4 cells (1×10^6) into the left lateral lobe of the liver in WT or *Nek2cKO* mice. As seen in the clinic, a single agent of αPD-1 had a minimal effect on the tumor inhibition. However, deletion of NEK2 in TAMs alone substantially inhibited the liver tumor growth, and its antitumor efficacy was greatly enhanced in combination with anti–PD-1 antibody treatment. While Hep-53.4 cells are known for their rapid growth and malignancy in orthotopic HCC tumor models, the combinatorial treatment substantially prolonged mouse mean overall survival from 17 days (control vehicle treatment) to 25 days. Either αPD-1 or *Nek2 cKO* alone failed to prolong the overall survival (Fig. 6, A to E). There was no substantial difference in spleen weight among the three groups at the end of treatment (Fig. 6F). Liver tumors in the *Nek2cKO* mice treated with anti–PD-1 antibody displayed a reduced number and altered phenotype of M2-like TAMs, increased infiltration and cytotoxic effects of $CD8^+$ T cells, and a shift from T_{regs} to a more T_H17-like phenotype in $CD4^+$ T cells (Fig. 6, G and H). Similar to the observations in the orthotopic model, αPD-1 treatment of *Nek2cKO* mice in the HTVi model substantially suppressed tumorigenesis and extended survival in tumor-bearing mice (Fig. 6, I to K), accompanied by a reversal of the immunosuppressive phenotype in HCC (Fig. 6, L to N). As expected, NEK2 depletion substantially decreased the levels of S1P in TAMs in both tumor tissue and serum (Fig. 6O).

Besides TAMs, NEK2 is mainly expressed in tumor cells (fig. S4C). Therefore, it was essential to know whether NEK2 deletion or inhibition alters tumor cell activities. Knockdown or inhibition of NEK2 in both Hep-53.4 and Hep3b cells had no notable effects on the proliferation and apoptosis of the tumor cells (fig. S10, A to D). To further determine the function of NEK2 in tumor cells on HCC growth, we generated a genetic mouse model, *Nek2f/f* × *AlbCre*, to knock out NEK2 in the tumor cells of HCC in vivo. We then investigated the effect of NEK2 depletion in tumor cells on tumor growth and the efficacy of ICB therapy. Unexpectedly, deletion of NEK2 in tumor cells did not attenuate tumor growth or enhance the therapeutic efficacy of αPD-1 in the orthotopic and HTVi models (fig. S10, E and F). Survival analyses showed that NEK2 deficiency combined with αPD-1 did not extend survival either (fig. S10G). These data together suggest that NEK2 inhibition in TAMs, but not in tumor cells, suppresses tumor progression and sensitizes HCC to PD-1–targeted immunotherapy.

Inhibition of S1P biosynthesis eradicates HCC in combination with ICB

In light of the above results that S1P metabolism contributed to immunotherapy-resistant HCC tumors, we reasoned that a S1P antagonist (fingolimod) in combination with ICB may enhance the therapeutic efficacy against HCC. To test this, we treated HTVi model HCC tumors with fingolimod plus anti–PD-1 antibody. As expected, the combination therapy had much greater antitumor efficacy in comparison with either fingolimod single agent or anti–PD-1 antibody alone, indicated by a more reduced number of tumors and lower liver weight and prolonged overall survival in the tumor-bearing mice (Fig. 7, A to C). In addition, the combination therapy did not affect the spleen weight of the mice, indicating the tolerability of treatment (fig. S11A). In the combination group, liver tumors exhibited a marked increase in the number and tumor killing capacity of cytotoxic T cells, while the proportion of exhausted T cells was reduced. In addition, the suppressive phenotypes of T_{regs} and TAMs were inhibited (fig. S11B).

As previously mentioned, we have identified NEK2 as a regulatory factor in S1P metabolism. Therefore, a NEK2 inhibitor represents another strategy to inhibit S1P biosynthesis. We additionally administrated NEK2 inhibitor and/or anti–PD-1 antibody to HTVi model HCC mice, after which both tumor number and tumor weight decreased substantially and overall survival was prolonged in mice that received the combined treatment (Fig. 7, D to F). There was no substantial difference in spleen weight between the groups at the end of treatment, and all groups were within the normal range for liver and kidney function (fig. S11, C and D). Hematoxylin and eosin staining of the spleen, kidney, and liver did not reveal notable differences between the groups (fig. S11E). Consistent with the tumor growth results, flow cytometric analysis demonstrated that the combination therapy group exhibited augmented infiltration levels and enhanced functional activity of tumor-infiltrating T lymphocytes, accompanied by a marked reduction in the frequency of exhausted T cell subsets. Notably, this therapeutic strategy induced a dual immunomodulatory effect through phenotypic reprogramming of immunosuppressive components: TAMs showed attenuated protumoral polarization, while T_{regs} displayed diminished suppressive capacity (Fig. 7G, and fig. S12, A and B). This combinatorial strategy was also verified in an orthotopic model, showing similar antitumor activity of the combination therapy (fig. S12, C to G). We observed that some mice in the combination therapy group remained tumor free. Specifically, initial subcutaneous implantation of Hep-53.4 cells followed by the combination immunotherapy had a higher CR rate to the treatment after secondary implantation with Hep-53.4 cells (Fig. 7H), indicating that combined treatment with a NEK2 inhibitor and an anti–PD-1 antibody induced both immediate antitumor activity and long-term immune memory.

Furthermore, we found that the efficacy of the combination therapy in orthotopic mice was substantially reduced when macrophages were precleared by clodronate liposomes and then reconstructed with WT or SPTLC1-KO macrophages (fig. S13, A to D). A similar result was seen in the HTVi model (fig. S13, E to H), showing that the

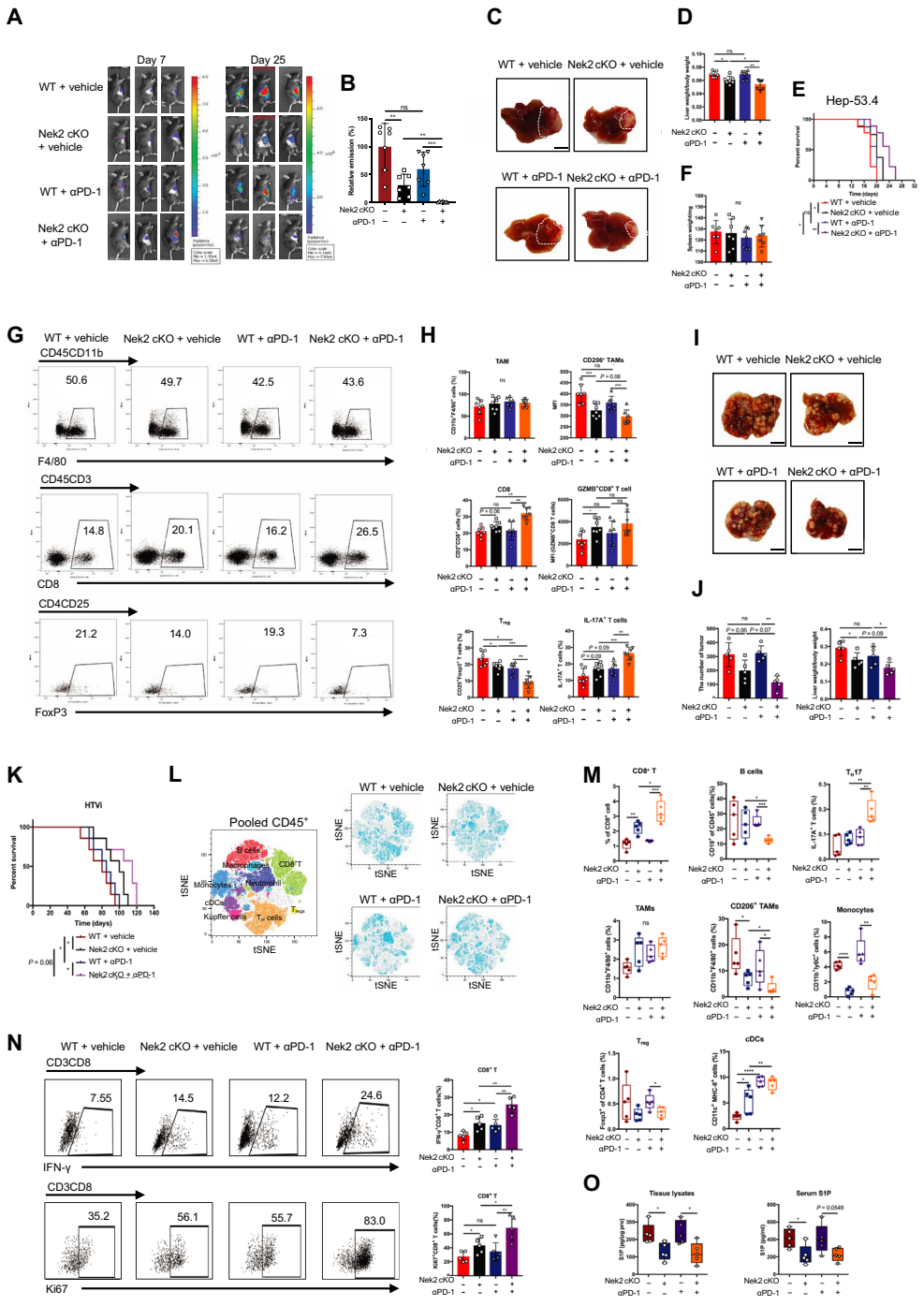

Fig. 6. NEK2 deficiency in TAMs sensitizes PD-1–targeted HCC immunotherapy. (**A** and **B**) Representative photograph and statistical results of the IVIS imaging system in mice orthotopically implanted with luciferase-expressing Hep-53.4 in *Nek2cKO* genetic mice in combination with αPD-1 treatment (200 μg per mouse, every 2 days, ip) ($n = 7$). (**C** and **D**) Representative images and statistical results of tumor in *Nek2cKO* genetic mice in combination with αPD-1 treatment ($n = 7$). (**E**) Survival curve of orthotopic tumor implantation in *Nek2cKO* genetic mice ($n = 7$). (**F**) The statistical results of spleen weight of *Nek2cKO* genetic mice in combination with αPD-1 treatment ($n = 7$). (**G** and **H**) Representative images and statistical results of immune cells in *Nek2cKO* genetic mice in combination with αPD-1 treatment ($n = 7$). (**I** and **J**) Representative images displaying tumors, tumor weight, and mouse weight of *Nek2cKO* genetic mice treated with αPD-1(200 μg per mouse, every 2 days, ip) in the HTVi model ($n = 5$). (**K**) Survival curve of HTVi model in *Nek2cKO* genetic mice in combination with αPD-1 ($n = 9$). (**L**) Plots of t-distributed stochastic neighbor embedding (tSNE) showing the distinct immune landscape of tumors in the different treatment groups. (**M**) Proportions of immune cell types in the four treatment groups ($n = 5$). MHC-II, major histocompatibility complex class II. (**N**) Flow cytometric analysis and statistical results of functional indication of lymphocytes that have infiltrated the tumors ($n = 5$). (**O**) Concentration analysis of S1P by ELISA in tissue lysates and serum from *Nek2cKO* mice in combination with αPD-1. $^*P < 0.05$, $^{**}P < 0.01$, and $^{***}P < 0.001$. Using a two-tailed, unpaired Student's t test (O), using one way ANOVA, with post hoc comparisons conducted using Tukey's test [(B), (D), (F), (H), (J) and (M)] or log-rank test [(E) and (K)]. Data are from ≥3 independent experiments (mean ± SD).

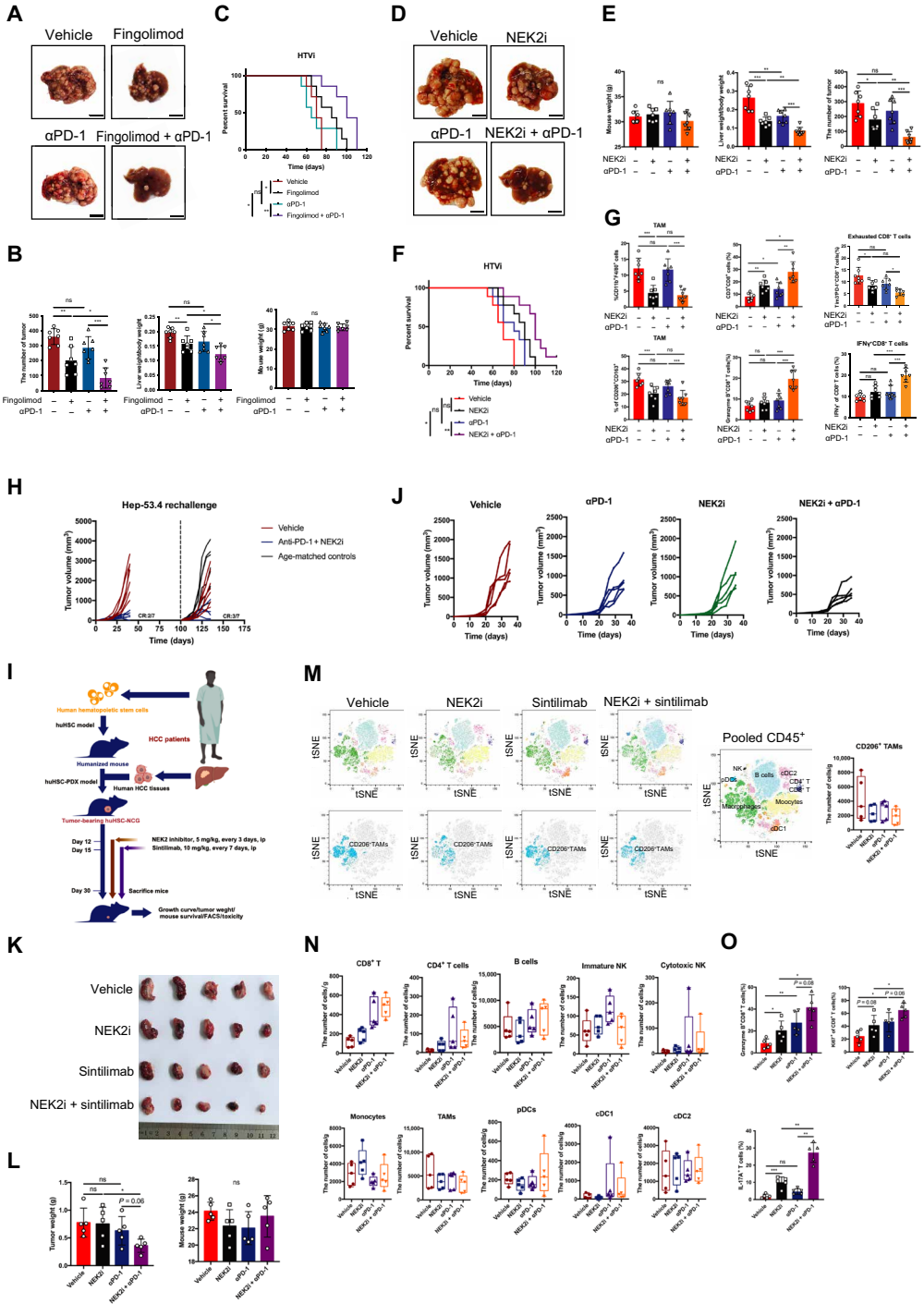

Fig. 7. The S1P antagonist or NEK2 inhibitor and PD-1 antagonist combination eradicates HCC in humanized mouse model. (**A** and **B**) Representative images and statistical results showing tumors harvested from the orthotopic model treated with the αPD-1 (200 μg per mouse, every 2 days, ip), fingolimod (10 mg/kg, every day, ip), or their combination ($n = 7$). (**C**) Survival curve of combination therapy in orthotopic model ($n = 7$). (**D** and **E**) Representative images and statistical results showing tumors harvested from the HTVi model treated with the αPD-1 (200 μg per mouse, every 2 days, ip), NEK2 inhibitor (5 mg/kg, every 2 days), or their combination ($n = 7$). (**F**) Survival curve of combination therapy in the HTVi model. (**G**) Statistical results of lymphocytes that have infiltrated the tumors ($n = 7$) by flow cytometric analysis. (**H**) Tumor growth curve of mice in individual groups is shown ($n = 7$). (**I**) Schematic protocol for combination therapy (NEK2 inhibitor: 5 mg/kg, every 3 days, ip; sintilimab: 10 mg/kg, every 7 days, ip) in the huHSC-NCG model. (**J** to **L**) Representative images displaying tumors, tumor volume, tumor weight, and mouse weight of combination therapy in huHSC-NCG model ($n = 5$). (**M**) Plots of tSNE showing the distinct immune landscape of tumors in the different treatment groups. (**N**) Proportions of immune cell types in the four treatment groups ($n = 5$). (**O**) Statistical results of functional indication of lymphocytes that have infiltrated the tumors in huHSC-NCG model ($n = 5$) by flow cytometric analysis. $^*P < 0.05$, $^{**}P < 0.01$, and $^{***}P < 0.001$. Using one-way ANOVA, with post hoc comparisons conducted using Tukey's test [(B), (E), (G), (L), (M), (N), and (P)] or log-rank test [(C) and (F)]. Data are from ≥3 independent experiments (mean ± SD).

efficacy of the combination therapy solely depends on the NEK2-SPTLC1 signaling pathway in TAMs. Moreover, the therapeutic efficacy of the NEK2 inhibitor and anti–PD-1 in Hep-53.4 tumor–bearing mice was entirely nullified by depleting macrophages using clodronate liposomes. In contrast, depletion of $CD8^+$ T cells or NK cells resulted in only partial attenuation of the antitumor effect (fig. S14, A and B). Flow cytometry confirmed immune cell depletion at the study endpoint (fig. S14C). These findings underscore the pivotal role of macrophages in shaping the tumor immune microenvironment, surpassing the contributions of $CD8^+$ T cells and NK cells alone. No notable signs of systemic intolerance (abnormal death or notable body weight changes), as well as spleen tissue histological changes, were observed in these treatments and depletion antibodies (fig. S14, D and E).

To evaluate the effect of the combination strategy in patients with HCC, we established a huHSC-NCG humanized mouse model for further preclinical test (Fig. 7I). In line with the results from the above-mentioned immunocompetent mouse tumor models, the combination of NEK2 inhibitor and sintilimab (αPD-1) substantially reduced tumor weight and volume, while NEK2 inhibitor or αPD-1 treatment alone only provided marginal therapeutic benefit (Fig 7, J to L). To exclude potential toxicity induced by the combination therapy, we evaluated the weight of the spleen and kidney and performed liver and kidney function tests. No notable toxicity was observed at the end of treatment (fig. S15, A to C). In line with the tumor growth phenotype, flow cytometrical analysis showed that the percentages of $CD206^+CD68^+$ cells decreased in tumors treated with the NEK2 inhibitor, sintilimab, or the combination therapy compared to the control group. In contrast, the percentages of $GZMB^+CD8^+$ T cells and $Ki67^+CD8^+$ T cells increased, while the percentages of $CD4^+$ T cells, B cells, NK cells, monocytes, and dendritic cells did not change substantially (Fig. 7, M to O, and fig. S15D).

In summary, our study demonstrated that NEK2-mediated S1P metabolic reprogramming in macrophages plays a crucial role in immune suppression and therapeutic resistance. Mechanistically, NEK2 enhances the activity of SPT by interacting with SPTLC1 through competitive occupancy of the negative regulator ORMDL3 and phosphorylating the S401 residue of SPTLC1 inside the ER lumen. S1P serves as a great indicator for prognosis and immunotherapy response in liver cancer. Combining the NEK2 inhibitor or the S1P antagonist with ICB provides notable antitumor efficacy by reprogramming the TME (Fig. 8).

DISCUSSION

Recent studies have revealed that distinct subsets of TAMs exhibit unique metabolic characteristics, which are pivotal in creating an immunosuppressive microenvironment and fostering resistance to immunotherapy (*3*). Therefore, it is crucial to identify specific metabolites and key enzymes capable of reshaping the metabolic profiles of macrophages. This transformation could potentially convert immunosuppressive TAM subsets into antitumor macrophages, thereby overcoming resistance to immunotherapy. Clinical trials of drug-eluting bead transarterial chemoembolization (DEB-TACE) have demonstrated notable depletion of immune cells, complicating the identification of drivers of immune resistance through multiomic analysis of biopsy specimens before surgery or chemotherapy (*30*). Unfortunately, the scarcity of tissue in biopsies limits the feasibility of this approach. To address this challenge, we developed a humanized mouse model to replicate the immunotherapy process for liver cancer in clinical scenarios without chemotherapy. Our investigations identified a group of Sphinx-like macrophages with active sphingolipid metabolism in liver cancer [sphingolipids were named as unusual "Sphinx-like" lipids by Johann Thudichum after the Greek mythical creature (*31*) and pinpointed S1P derived from TAMs and NEK2 within TAMs as pivotal factors driving immunotherapy resistance at metabolic and genetic levels, respectively]. Specifically, our findings suggest that NEK2 enhances S1P synthesis, akin to an accelerator increasing fuel supply in a vehicle, thereby intensifying tumor immunotherapy resistance.

Previous studies have highlighted the role of S1P role in various liver diseases. For instance, plasma S1P levels are notably diminished in patients with hepatopulmonary syndrome, particularly in severe cases (*32*). In addition, S1P is implicated in the activation and differentiation of HSCs into myofibroblasts, thereby contributing to liver fibrosis (*10*). Moreover, the S1P/S1PR1 pathway has been linked to the promotion of both primary and metastatic tumor growth within the congestive liver environment (*14*). Our own findings corroborate that S1P metabolism directly induces mitochondrial OXPHOS and fosters an immunosuppressive phenotype in TAMs and T_{regs}. Furthermore, it attenuates proliferation and energy metabolism while promoting exhaustion in $CD8^+$ T cells. Drawing from prior research (*13*, *33*, *34*), we hypothesize that S1P's regulation of TAMs operates through two primary mechanisms. First, S1P synthesized within TAMs is directly shuttled to mitochondria to support OXPHOS. Second, extracellular S1P, originating from immune and tumor cells, binds to S1P receptors, triggering intracellular signaling pathways. These hypotheses necessitate further validation through forthcoming experiments.

S1P antagonists and SPT inhibitors have been extensively studied in non-neoplastic diseases and hematological malignancies (*35*–*37*). Notably, the S1P receptor antagonist fingolimod has undergone numerous clinical trials for conditions such as multiple sclerosis, schizophrenia, acute optic neuritis, and severe COVID-19 (*38*–*42*), underscoring the therapeutic potential of targeting S1P metabolism across diverse diseases. In our prior research, we demonstrated that NEK2 interacts with and phosphorylates PD-L1 at residues T194/T210, thereby stabilizing PD-L1; inhibition of NEK2 accelerates PD-L1 degradation, activating cytotoxic T cells to eliminate pancreatic cancer cells (*28*). In this study, we extend these findings to TAMs associated with HCC, suggesting NEK2 targeting for immunotherapy across multiple tumor types, although the detailed regulatory mechanisms remain to be elucidated. Mechanistically, NEK2 enhances SPT activity by alleviating ORMDL3-mediated inhibition and directly phosphorylating SPTLC1, thereby increasing S1P synthesis. Unlike SPT inhibitors, NEK2 targeting may selectively disrupt these regulatory interactions, offering more precise control over S1P production. While S1P receptor inhibitors block downstream signaling pathways, they do not affect S1P synthesis, potentially leaving other S1P-mediated processes unaffected. Therefore, NEK2 inhibitors represent a promising therapeutic strategy with broader applicability compared to SPT and S1P receptor inhibitors, which require extensive preclinical validation in both in vivo and in vitro tumor models.

In conclusion, we have identified two prognostic and immunotherapy response indicators in liver cancer: $NEK2^{hi}$ TAMs within tumor tissues and elevated S1P levels in serum. Our study has uncovered a mechanism underlying the tumor-suppressive microenvironment and immunotherapy resistance: NEK2 enhances SPTLC1

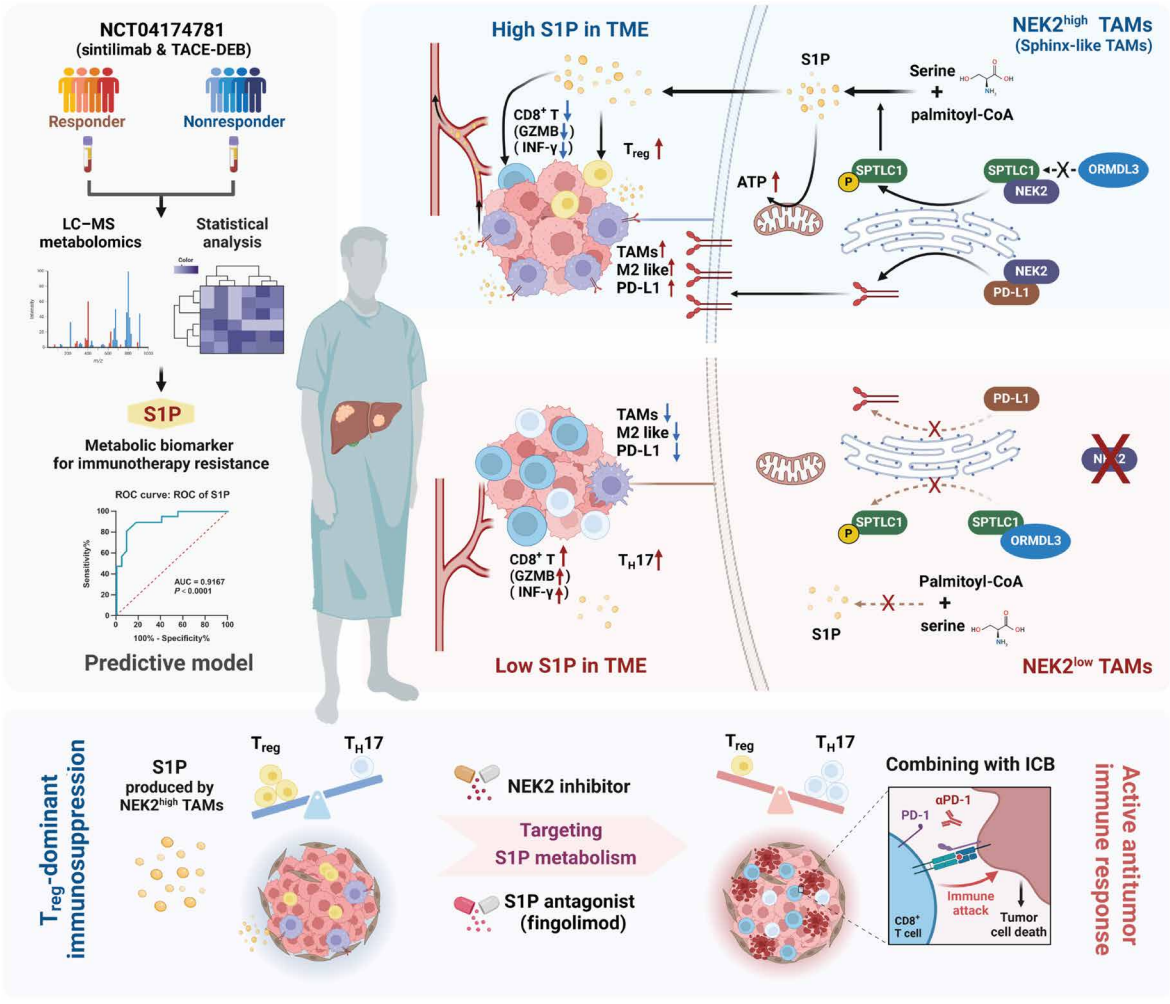

Fig. 8. Predicted model of the NEK2-mediated sphingolipid synthesis in macrophages. A schematic model is proposed to illustrate how tumor immune surveillance and therapeutic resistance are regulated by NEK2-mediated sphingolipid synthesis in macrophages. Combining the NEK2 inhibitor or S1P antagonist with ICB provides notable antitumor efficacy by reprogramming the TME.

metabolic activity by interacting with SPTLC1, competitively displacing the negative regulator ORMDL3 and phosphorylating SPTLC1 at the S401 residue within the ER lumen. Furthermore, NEK2 upregulates PD-L1 expression in TAMs. Last, we propose a synergistic therapeutic approach that combines targeting S1P metabolism with NEK2 inhibitors for enhancing immunotherapy efficacy in HCC.

MATERIALS AND METHODS

Study design

The goal of this study is to identify clinical indicators of prognosis and immunotherapy response, develop therapeutic strategies for HCC, and enhance the efficacy of immunotherapy. We initially conducted a metabolomic analysis of serum from patients with HCC involved in a clinical trial (NCT04174781) and human HCC tumors derived from humanized mouse orthotopic HCC models treated with an anti–PD-1 monoclonal antibody, comparing responder and nonresponder groups. Our findings indicate that S1P levels serve as a robust clinical indicator for prognosis and immunotherapy response in patients with HCC. To determine the primary cellular sources of S1P production, we assessed the enzymatic activity of SPT using a specific assay and measured S1P levels via ELISA. We determined that TAMs are a primary source of secreted S1P in the TME. To investigate the role of TAMs in ICB resistance and tumor progression, we isolated macrophages from tumors of the same humanized mouse models treated with sintilimab. RNA-seq analysis of TAMs from responders and nonresponders revealed that the *NEK2* gene was one of the top-ranked genes exhibiting substantially increased expression in TAMs from nonresponders. mIHC of human HCC tumor tissues confirmed that NEK2 was coexpressed with SPTLC1 (an SPT isoform) in TAMs. Given the correlation between S1P metabolism and NEK2 in TAMs, we hypothesized that NEK2 may act as a direct or indirect regulator of S1P-related metabolism. To test this hypothesis, we performed MS-based metabolite profiling, ELISA, and SPT enzymatic activity assessments on WT and NEK2-KO TAMs, as well as on TAMs treated with a NEK2 inhibitor. The results indicated that NEK2^{hi} TAMs are the primary source of S1P in HCC tumors. We used mouse models and cell biology assays to confirm the physiological effects of NEK2-induced sphingolipid synthesis in TAMs on HCC tumor growth and the TME. The molecular

mechanisms underlying NEK2 regulation of sphingolipid synthesis were elucidated through biochemical and molecular biological analyses. We evaluated the metabolic characteristics of immune cells regulated by NEK2-mediated sphingolipid synthesis using metabolomic analysis, TEM, mitochondrial assays, and Seahorse assays. Combination therapy involving a NEK2 inhibitor and anti–PD-1 antibody was tested in various mouse models, including the HTVi model, orthotopic injection model, and huHSC-NCG humanized mouse model. In all animal experiments, animals were randomly assigned to treatment groups without blinding due to the complexity of the experimental design, limited researchers, and poor feasibility of blinding; sample sizes are specified in each figure legend. Appropriate statistical tests were applied for every figure, and all data met the assumptions of these tests. Although we did not use statistical methods to predetermine sample sizes, our sample sizes align with those commonly used in the field. All in vitro experiments were conducted independently at least three times, with no samples or animals excluded from our analyses.

Human tissues

Human HCC tissue specimens were obtained from the Department of Hepatobiliary and Pancreatic Surgery, the First Affiliated Hospital, School of Medicine, Zhejiang University. The protocol was approved by the Institutional Review Board at the First Affiliated Hospital, School of Medicine, Zhejiang University (approval number: 1474). Written informed consent was obtained from each patient at the time of enrollment. Blood samples were collected from patients with HCC and benign before surgery or before TACE-DEB and TACE-DEB plus αPD-1 treatments in a clinical trial (NCT04174781) separated from serum and stored at −80°C. Patients had HCC of Barcelona clinic liver cancer (BCLC) stage A who exceeded the Milan criteria or had BCLC stage B, and all patients had Child-Pugh A liver function and did not have vascular invasion, extrahepatic metastasis, or clinically notable portal hypertension. Sixty-one patients enrolled, all of whom underwent at least one treatment cycle combining DEB-TACE and sintilimab.

Animals

Nek2f/f, Lyz2cre, AlbCre, Clec4fCre, C57BL/6, Balb/c nude, and humanized mice were obtained from GemPharmatech. All animal experiments were performed in the Experimental Animal Center, the First Affiliated Hospital, School of Medicine, Zhejiang University. Mice of both genders (4 to 6 weeks of age) were used. Animal protocols were approved by the Ethics Committee of the First Affiliated Hospital, School of Medicine, Zhejiang University (approval number: 1488).

Cell lines

THP1 (TIB-202), RAW264.7 (TIB-71), Hep-53.4 (400200), and Hep3B (HB-8064) cell lines were obtained from the American Type Culture Collection. These cell lines were cultured in a complete medium consisting of RPMI 1640 with 2 mM L-glutamine, penicillin-streptomycin (100 U/ml), and 10% fetal bovine serum (FBS). The cells were passaged up to 20 times and maintained at 37°C and 5% CO_2.

Transmission electron microscopy

Tumor-infiltrating macrophages were fixed in cold 2.5% glutaraldehyde in 10 mM phosphate-buffered saline (PBS) for 24 hours followed by washing, dehydrating, and embedding that reported previously (*7*). Fifty-nanometer-ultrathin sections were performed using a JEOL 1011 transmission electron microscope.

Histology and image analysis

Tissue samples were fixed in 4% paraformaldehyde for 48 hours, processed for paraffin embedding, and cut into 5-μm sections for immunofluorescence or hematoxylin and eosin staining as described previously (*43*). Imaging acquisition was performed using ImageScope software (Leica Biosystems). Staining performance was quantified by processing images using 3DHISTECH QuantCenter 2.1 software.

In vitro kinase assay

NEK2 (active) (Sigma-Aldrich) were incubated with SPTLC1 human recombinant protein (OriGENE) and 300-μm ATP (Cell Signaling Technology) in a kinase buffer (Cell Signaling Technology) at 30°C for 40 min. The kinase reaction was boiled with 1× SDS buffer and analyzed by immunoblotting.

GST pull-down assay

Commercial SPTLC1 (human) recombinant protein (P01) (Abnova), NEK2-His (LifeSpan Biosciences), and recombinant human GST (Abcam) were subjected to GST pull-down assay. The conjugation of GST and SPTLC1/GST with glutathione beads (Sigma-Aldrich) and the pull-down assay were performed using the Pierce GST Protein Interaction Pull-Down Kit (Thermo Fisher Scientific) according to the manufacturer's instructions. The assay reaction was stopped by the boiling of 1× SDS buffer and subsequently subjected to Western blotting.

Western blotting

Cell extracts were prepared following previously established methods (*28*). The samples were separated using SDS–polyacrylamide gel electrophoresis and transferred onto nitrocellulose membranes. The membranes were then blocked with 5% bovine serum albumin (Beyotime) and incubated with primary antibodies. Detection was performed with goat anti-mouse or anti-rabbit horseradish peroxidase–conjugated secondary antibodies (Beyotime). Immunoreactive protein signals were detected using ECL Detection Reagent (Merck Millipore), and the resulting bands were visualized with ChemiScopeTouch (Clinx Science Instruments).

Trypsinization of ER microsomal fractions

ER fraction was collected from tumor-infiltrating macrophages cells by an ER enrichment kit (Novus Biologicals). After pretreatment with or without 1% Triton X-100 (Beyotime) for 5 min, ER fraction in the reaction buffer [trypsin (0.625 g/liter) + EDTA (0.05 g/liter) in PBS] was incubated for the indicated time. After trypsinization, samples were stopped by the boiling of 1× SDS buffer and analyzed by Western blotting with primary antibodies against IRE1α (Cell Signaling Technology), HSP90B1 (Novus Biologicals), epidermal growth factor receptor (Cell Signaling Technology), NEK2 (Santa Cruz), and α-tubulin (Abcam).

Duolink proximity ligation assay

A Duolink proximity ligation assay between NEK2 and SPTLC1 was performed by a Duolink in situ proximity ligation assay kit (Sigma-Aldrich, DUO92101) according to the manufacturer's instructions.

Cell isolation and flow cytometry

Tumors were mechanically minced into a homogenate, placed in RPMI with 2% FBS, and filtered through a 45-μm cell strainer. The filtered cells were resuspended in a 36% Percoll solution (GE Healthcare) containing 4% 10× PBS and 60% serum-free Dulbecco's modified

Eagle's medium and then separated using density gradient centrifugation to remove non-immune cells. The enriched leukocytes were incubated with lysing buffer (BD Biosciences) to lyse red blood cells and then washed with fluorescence-activated cell sorting (FACS) buffer (PBS + 1% FBS + 0.1% sodium azide).

For surface staining, cells were blocked with TruStain FcX (5 μg/ml; anti-mouse CD16/32) antibody (BioLegend) at 4°C for 15 min before staining. Cell suspensions were first stained using the LIVE/DEAD Fixable Violet Dead Cell Stain Kit (Thermo Fisher Scientific) on ice for 15 min in the dark. After washing, surface proteins were stained for 25 min at 4°C. For intracellular cytokine staining [tumor necrosis factor–α, interferon-γ (IFN-γ), GZMB, and IL-17A], immune cells were incubated for 4 to 6 hours at 37°C with phorbol 12-myristate 13-acetate (50 ng/ml; Sigma-Aldrich), ionomycin (750 ng/ml; Sigma-Aldrich), and brefeldin A (10 μg/ml; Sigma-Aldrich) before being stained according to the manufacturer's instructions using the Cytofix/Cytoperm fixation/permeabilization kit (BD Biosciences).For transcription factor staining (FoxP3 and Ki67), cells were fixed and permeabilized using the Foxp3/transcription factor staining buffer set, following the manufacturer's instructions (eBioscience).

All samples were analyzed using a BD LSRFortessa (BD Biosciences) and a Cytek Aurora full spectrum flow cytometer (Cytek Biosciences). The data were further analyzed with FlowJo software (Becton Dickinson).

In vitro T cell proliferation assay

Mouse splenic $CD8^+$ T cells from OT-I mice were isolated using a $CD8^+$ T cell isolation kit (Miltenyi Biotec) and then labeled with CFSE (Invitrogen) in PBS for 10 min at 37°C according to the manufacturer's instructions. The CFSE-labeled $CD8^+$ T cells (0.5×10^5 per well) were cultured in plate-bound αCD3 (2 μg/ml; BioLegend) and αCD28 (5 μg/ml; BioLegend) with complete RPMI medium containing 20 μM S1P or isolation WT, and *Nek2cKO* TAMs were added in the plates and coincubated with T cells at a ratio of 1:8 (TAMs:T cells) for 3 days. Cells were then harvested, and the CFSE-positive signal in the $CD8^+$ gate was measured by FACS (BD LSRFortessa).

T_{reg} suppression assays

Naive $CD4^+$ T cells were enriched from the spleen of 6-week-old mice using the $CD4^+$ T Cell Isolation Kit (Miltenyi Biotec), and their purity was checked by flow cytometry. Naive $CD4^+$ T cells were incubated with plate-bound αCD3 (5 μg/ml; BioLegend) and αCD28 (3 μg /ml; BioLegend) in the presence of IL-2 (3 ng/ml; PeproTech) and transforming growth factor–β (5 ng/ml; PeproTech). For mouse T_{reg} suppression assays, T_{regs} were cultured with WT and *Nek2cKO* TAMs or in the presence of 20 μM S1P for 24 hours before being cultured with $CD8^+$ T cells, and the proliferation of $CD8^+$ T cells was determined by CFSE dilution with flow cytometry analysis.

OT-1 cell–mediated tumor cell destruction assay

OT-1 cells were isolated from the mouse spleen using a $CD8^+$ T cell isolation kit, a large size (LS) column, and a MidiMACSTM separator. OT-1 cells were activated by plate-bound αCD3 (2 μg/ml; BioLegend), αCD28 (5 μg /ml; BioLegend), and recombinant murine IL-2 (10 ng/ml; PeproTech) in RPMI 1640 supplemented with 10% FBS and 1% antibiotic mixture for 3 days. Hep-53.4 ovalbumin (OVA) were permitted to adhere to the plates overnight and then incubated for 48 hours with activated OT-1 cells after coculturing with WT or *Nek2cKO* TAMs (or TAMs pretreated with the NEK2 inhibitor). The ratio between Hep-53.4 OVA and activated OT-1 cells was 1:3 to 1:5. OT-1 cells, and cell debris were removed and washed three times using PBS. The remaining living cancer cells were fixed with 4% paraformaldehyde, stained with 0.5% crystal violet, and quantified percentage of tumor cell death.

Proteomic and phosphoproteomic analysis of TAMs

MS analysis was performed by PTM-Biolabs Co. Ltd. (Hangzhou, China). The experimental protocol was conducted as previously described (*28*).

Metabolic analysis

Seahorse XFp metabolic assays

For real-time analysis, ECAR and OCR were measured with an XF24 extracellular fluxanalyser (Agilent) following the manufacturer's protocols. Briefly, cells were treated with oligomycin (1 μM, Cayman), carbonyl cyanide *p*-trifluoromethoxyphenylhydrazone (2 μM, MedChemExpress), rotenone (1 μM, MedChemExpress), antimycin A (0.5 μM, Cayman), glucose (10 mM, MedChemExpress), and 2-deoxyglucose (50 mM, MedChemExpress). Each condition was analyzed, with three to six replicates in each single experiment.

Nontarget metabolomic analysis

All chemicals and solvents used were of analytical or high-performance liquid chromatography grade. We isolated 1×10^7 macrophage cells from the bones of 6-week-old Nek2f/f and *Nek2f/f* × *lyz2Cre* mice. TAMs were stimulated with Hep-53.4 conditioned medium for 24 hours. Each sample was mixed with 1 ml of methanol (4:1, v/v) and transferred to a 4-ml glass vial. Then, 200 μl of chloroform was added to each aliquot, and the samples were dispersed by pipetting. The cells were disrupted using an ultrasonic homogenizer for 6 min at 500 W. All mixtures were transferred to 1.5-ml Eppendorf tubes, with 20 μl of L-2-chlorophenylalanine (0.3 mg/ml) in methanol added as an internal standard. The samples were extracted by ultrasonication for 20 min in an ice water bath, followed by centrifugation at 4°C (13,000 rpm) for 10 min. The supernatant (800 μl) was dried in a freeze concentration centrifugal dryer. A 300-μl mixture of methanol and water (1:4, v/v) was added to each sample, vortexed for 30 s, sonicated for 3 min in an ice water bath, and then placed at −20°C for 2 hours. The samples were centrifuged at 4°C (13,000 rpm) for 10 min, and 150 μl of the supernatant from each tube was collected using crystal syringes, filtered through 0.22-μm microfilters, and transferred to liquid chromatography (LC) vials. The vials were stored at −80°C until LC-MS analysis. The samples were analyzed using an ACQUITY UPLC I-Class system (Waters Corporation, Milford, USA) coupled with a VION IMS QTOF mass spectrometer (Waters Corporation, Milford, USA).

Energy metabolomic analysis

The sample was thawed on ice, and 100 μl of ultrapure water extract was added to resuspend the cell pellet. Fifty microliters of cell suspension was divided, and 200 μl of methanol (precooled at −20°C) was added and vortexed for 2 min under the condition of 2500 rpm. The sample was frozen in liquid nitrogen for 5 min and removed on ice for 5 min, after that, the sample was vortexed for 2 min. The previous step was repeated for three times. The sample was centrifuged at 12,000 rpm for 10 min at 4°C. Two hundred microliters of the supernatant was taken into a new centrifuge tube, and the supernatant was placed in −20°C refrigerator for 30 min. Then, the supernatant was centrifuged at 12,000 rpm for 10 min at 4°C. After

centrifugation, 180 μl of the supernatant was transferred through protein precipitation plate for further LC-MS analysis. The left 50-μl cell suspension was frozen, thawed for three times, and centrifuged at 12,000 rpm for 10 min, and the supernatant was taken to determine the protein concentration by a BCA Protein Assay kit. The sample extracts were analyzed using an LC–electrospray ionization–tandem MS system (Waters ACQUITY H-ClassD, MS, QTRAP 6500+ System).

Preparation of macrophages from bone marrow and macrophage activation

After isolation from the mouse femur, bone marrow cells were differentiated for 7 days in the presence of recombinant mouse macrophage colony-stimulating factor (M-CSF; 20 ng/ml; PeproTech) in a complete medium [RPMI 1640 with penicillin-streptomycin (100 U/ml) and 10% FBS]. On day 7, the macrophages were washed and stimulated with IL-4 (20 ng/ml; PeproTech) or a combination of lipopolysaccharide (20 ng/ml; Sigma-Aldrich) and IFN-γ (50 ng/ml; PeproTech). After 24 hours, the macrophages were collected and analyzed by flow cytometry for M2 or M1 activation markers. In addition, TAMs were stimulated with Hep-53.4 conditioned medium for 24 hours.

Tumor-bearing mouse models

HTVi-induced HCC model

Mouse primary liver tumors were induced by HTVi of oncogenes including PT3-EF1a-C-Myc and PT/Caggs-NRas-V12 (Ras/Myc), combined together with the sleeping beauty transposase, pCMV-SB11, which were obtained from Addgene. Plasmid DNAs were diluted in PBS and injected at 0.1 ml/g body weight of mice through the tail vein in 7 to 8 s.

Orthoptic-HCC model

To establish orthotopic models, 5- to 8-week-old C57BL/J male mice were anesthetized with pentobarbital sodium and subjected to a surgical procedure. After middle abdominal incision, the left lateral lobe was exposed and injected with 1×10^6 tumor cells resuspended in cold PBS mixed at 1:1 dilution with Matrigel (Corning) in a final volume of 25 μl. Mice were monitored with ultrasound imaging to measure tumor progression. Experiments were terminated when tumors reached a size of 1000 mm^3, as per the Institutional Animal Care and Use Committee limit.

huHSC NCG-HCC PDX model

huHSC-NCG(CH) mice(strain no. T037620)were purchased from GemPharmatech (Nanjing, China). All patient-derived xenografts (PDXs) were obtained from Department of Hepatobiliary and Pancreatic Surgery, the First Affiliated Hospital, School of Medicine, Zhejiang University. All PDXs were propagated in NCG mice, harvested, and implanted into female huHSC-NCG mice for 6 weeks. All HCC PDXs used in this study were from passages F1 to F3. Briefly, tumor tissues were minced to a size of 3 mm by 3 mm and were implanted subcutaneously through a tiny incision in the right flank of anesthetized huHSC-NCG mice. Two perpendicular tumor diameters were measured twice per week, and the tumor surface area was calculated according to a formula 1/2 (length × $width^2$). All experiments were performed in a specific pathogen–free grade facility, in which the mice were housed in prepackaged disposable irradiated cages and fed an irradiated diet and acidified water.

Macrophage depletion and reconstitution in a mouse model

The depletion/reconstitution protocol has several steps, including clodronate liposomes–induced macrophage depletion in mice, condition KO (cKO) BMDM preparation, and reconstitution of the mice with cKO BMDMs that reported previously (*44*). Briefly, to deplete macrophages, the clodronate-containing liposomes (5 mg/ml, Yeasen) or control liposomes (5 mg/ml, Yeasen) (200 μl per mouse) need to be delivered to the mice intravenously by a 1-ml syringe with a 28-gauge needle. Elimination of macrophages can be confirmed by analyzing $F4/80^+$ resident macrophages in the spleen using FACS assays after 48 hours. Two days after clodronate liposome treatment, the macrophage-depleted mouse can be reconstituted with new macrophages. After isolation from the WT or *Nek2cKO* mice (or Sptlc1 KO) femur, bone marrow cells were differentiated for 7 days in the presence of recombinant mouse M-CSF (20 ng/ml; PeproTech) in a complete medium [RPMI 1640 with penicillin-streptomycin (100 U/ml) and 10% FBS]. After 24 hours, the macrophages were collected and subjected to Western blot analysis to verify the KO of Nek2 or Sptlc1. Mono-macrophages (2×10^6 each mouse/200 μl) were subsequently transferred to the macrophage-cleared mice via intravenous injection (tail vein intravenously).

Protein-protein interaction measurements by MST assay

NEK2-SPTLC1 interaction measurements by MST assay was performed by Wuhan Bio-Lab biotechnology. Briefly, the human recombinant NEK2 protein (Abcam, ab42599) was labeled according to the protocol of protein labeling kit RED-NHS (Nanotemper, catalog no. Mo-L018). The tested SPTLC1 protein (4.8 μM) was also diluted into the 1× Tris-NaCl-Tween (TNT) buffer [10 mM tris-HCl, 0.15 M NaCl, and 0.5% Tween 20 (pH 7.8 to 8.2)] (Sangon Biotech Co. Ltd., Shanghai; cat. no. B548108) for the final MST assay. The MST experiment was performed using the Monolith NT.115 instrument (NanoTemper Technologies). The labeled NEK2 protein (400 nM) was mixed with the indicated concentrations of candidate sptlc1 protein in reaction buffer containing 1× TNT buffer [10 mM tris-HCl, 0.15 M NaCl, and 0.5% Tween 20 (pH 7.8 to 8.2)] (Sangon Biotech Co. Ltd., Shanghai; cat. no. B548108). The MST data were then collected under 40% infrared laser power and 100% light-emitting diode power. The data were analyzed by NanoTemper analysis software (v.2.3), and the K_d was determined.

Antibody generation and detection of anti–phospho-S401-SPTLC1 antibodies

To generate custom antibodies against phosphorylation S401 SPTLC1 using single B cell antibody technologies, a 16- to 24-week process comprising five phases was conducted, as follows:

Phase 1 (2 to 3 weeks) antigen preparation: The design and synthesis of the S401-SPTLC1 peptide.

Phase 2 (8 to 9 weeks) antigen immunization: Conjugated peptides were then used to immunize rabbits through five rounds of immunization in phase 2.

Phase 3 (1 to 2 weeks) FACS sorting for memory B cells: After immunization, the splenocytes and peripheral blood mononuclear cells are then harvested for FACS to isolate any antibody secreting B cells.

Phase 4 (5 to 6 weeks) B cell cloning: Following FACS sorting, the B cells can be directly lysed for gene amplification; alternatively, the B cells may be expanded in vitro, and the cell culture supernatants were analyzed using ELISA or FACS assays. Once any positive clones have been selected, the antibody variable genes are amplified.

Phase 5 (1 to 2 weeks) Antibody expression and validation: The antibodies are then recombinantly expressed in a mammalian cell line and fully validated.

Molecular docking analysis

Rigid protein-protein docking was performed between NEK2 and SPT complex to investigate the relationships by using GRAMM-X (http://gramm.compbio.ku.edu/). The protein structural domains of human serine palmitoyltransferase complex (SPTLC1/SPLTC2/ssSPTa/ORMDL3) [Protein Data Bank (PDB) ID: 7K0M] and NEK2 (PDB ID: 2XNM) were obtained from the PDB database (http://rcsb.org/). The PyMOL (version: 2.2.7) software was used to depict the interaction details of the docking model as a three-dimensional graphic for the docking results.

Statistical analysis

Data analysis was performed using GraphPad Prism software (v.9, GraphPad Inc., La Jolla, CA, USA). Results are presented as means ± SD, based on at least three replicates. Differences between two groups were evaluated using either Mann-Whitney *U* tests or two-sided Student's *t* tests, depending on the data distribution. Correlations between variables were assessed using Spearman's rank correlation. The overall differences at the endpoint for tumor growth were determined using Student's *t* tests. Survival curve differences between groups were analyzed using the Kaplan-Meier method and the Gehan-Breslow-Wilcoxon test. Statistical significance was defined as $*P < 0.05$, $**P < 0.01$, $***P < 0.001$, and $****P < 0.0001$.

Supplementary Materials

This PDF file includes:

Figs. S1 to S15
Tables S1 to S5

REFERENCES AND NOTES

1. F. Bray, M. Laversanne, H. Sung, J. Ferlay, R. L. Siegel, I. Soerjomataram, A. Jemal, Global cancer statistics 2022: GLOBOCAN estimates of incidence and mortality worldwide for 36 cancers in 185 countries. *CA Cancer J. Clin.* **74**, 229–263 (2024).
2. R. Noy, J. W. Pollard, Tumor-associated macrophages: From mechanisms to therapy. *Immunity* **41**, 49–61 (2014).
3. I. Vitale, G. Manic, L. M. Coussens, G. Kroemer, L. Galluzzi, Macrophages and metabolism in the tumor microenvironment. *Cell Metab.* **30**, 36–50 (2019).
4. A. Christofides, L. Strauss, A. Yeo, C. Cao, A. Charest, V. A. Boussiotis, The complex role of tumor-infiltrating macrophages. *Nat. Immunol.* **23**, 1148–1156 (2022).
5. J. Xiao, S. Wang, L. Chen, X. Ding, Y. Dang, M. Han, Y. Zheng, H. Shen, S. Wu, M. Wang, D. Yang, N. Li, C. Dong, M. Hu, C. Su, W. Li, L. Hui, Y. Ye, H. Tang, B. Wei, H. Wang, 25-Hydroxycholesterol regulates lysosome AMP kinase activation and metabolic reprogramming to educate immunosuppressive macrophages. *Immunity* **57**, 1087–1104. e7 (2024).
6. L. Wu, X. Zhang, L. Zheng, H. Zhao, G. Yan, Q. Zhang, Y. Zhou, J. Lei, J. Zhang, J. Wang, R. Xin, L. Jiang, J. Peng, Q. Chen, S. M. Lam, G. Shui, H. Miao, Y. Li, RIPK3 orchestrates fatty acid metabolism in tumor-associated macrophages and hepatocarcinogenesis. *Cancer Immunol. Res.* **8**, 710–721 (2020).
7. L. N. Raines, H. Zhao, Y. Wang, H. Y. Chen, H. Gallart-Ayala, P. C. Hsueh, W. Cao, Y. Koh, A. Alamonte-Loya, P. S. Liu, J. Ivanisevic, C. W. J. Lio, P. C. Ho, S. C. C. Huang, PERK is a critical metabolic hub for immunosuppressive function in macrophages. *Nat. Immunol.* **23**, 431–445 (2022).
8. Y. Xiong, W. Piao, C. C. Brinkman, L. Li, J. M. Kulinski, A. Olivera, A. Cartier, T. Hla, K. L. Hippen, B. R. Blazar, S. R. Schwab, J. S. Bromberg, CD4 T cell sphingosine 1-phosphate receptor (S1PR)1 and S1PR4 and endothelial S1PR2 regulate afferent lymphatic migration. *Sci Immunol.* **4**, eaav1263 (2019).
9. A. Baeyens, S. Bracero, V. S. Chaluvadi, A. Khodadadi-Jamayran, M. Cammer, S. R. Schwab, Monocyte-derived S1P in the lymph node regulates immune responses. *Nature* **592**, 290–295 (2021).
10. S. L. Friedman, Mechanisms of hepatic fibrogenesis. *Gastroenterology* **134**, 1655–1669 (2008).
11. Y. Takuwa, Y. Okamoto, K. Yoshioka, N. Takuwa, Sphingosine-1-phosphate signaling and biological activities in the cardiovascular system. *Biochim. Biophys. Acta* **1781**, 483–488 (2008).
12. S. Ma, R. Sandhoff, X. Luo, F. Shang, Q. Shi, Z. Li, J. Wu, Y. Ming, F. Schwarz, A. Madi, N. Weisshaar, A. Mieg, M. Hering, F. Zettl, X. Yan, K. Mohr, N. ten Bosch, Z. Li, G. Poschet, H. R. Rodewald, N. Papavasiliou, X. Wang, P. Gao, G. Cui, Serine enrichment in tumors promotes regulatory T cell accumulation through sphinganine-mediated regulation of c-Fos. *Sci. Immunol.* **9**, eadg8817 (2024).
13. P. Chakraborty, S. G. Vaena, K. Thyagarajan, S. Chatterjee, A. al-Khami, S. P. Selvam, H. Nguyen, I. Kang, M. W. Wyatt, U. Baliga, Z. Hedley, R. N. Ngang, B. Guo, G. C. Beeson, S. Husain, C. M. Paulos, C. C. Beeson, M. J. Zilliox, E. G. Hill, M. Mehrotra, X. Z. Yu, B. Ogretmen, S. Mehrotra, Pro-survival lipid sphingosine-1-phosphate metabolically programs T cells to limit anti-tumor activity. *Cell Rep.* **28**, 1879–1893.e7 (2019).
14. H. Kawai, Y. Osawa, M. Matsuda, T. Tsunoda, K. Yanagida, D. Hishikawa, M. Okawara, Y. Sakamoto, T. Shimagaki, Y. Tsutsui, Y. Yoshida, S. Yoshikawa, K. Hashi, H. Doi, T. Mori, T. Yamazoe, S. Yoshio, M. Sugiyama, D. Okuzaki, H. Komatsu, A. Inui, M. Tamura-Nakano, C. Oyama, H. Shindou, H. Kusano, M. Kage, T. Ikegami, K. Yanaga, T. Kanto, Sphingosine-1-phosphate promotes tumor development and liver fibrosis in mouse model of congestive hepatopathy. *Hepatology* **76**, 112–125 (2022).
15. E. L. Pearce, M. C. Poffenberger, C. H. Chang, R. G. Jones, Fueling immunity: Insights into metabolism and lymphocyte function. *Science* **342**, 1242454 (2013).
16. C. S. Field, F. Baixauli, R. L. Kyle, D. J. Puleston, A. M. Cameron, D. E. Sanin, K. L. Hippen, M. Loschi, G. Thangavelu, M. Corrado, J. Edwards-Hicks, K. M. Grzes, E. J. Pearce, B. R. Blazar, E. L. Pearce, Mitochondrial integrity regulated by lipid metabolism is a cell-intrinsic checkpoint for Treg suppressive function. *Cell Metab.* **31**, 422–437.e5 (2020).
17. S. K. Wculek, I. Heras-Murillo, A. Mastrangelo, D. Mañanes, M. Galán, V. Miguel, A. Curtabbi, C. Barbas, N. S. Chandel, J. A. Enríquez, S. Lamas, D. Sancho, Oxidative phosphorylation selectively orchestrates tissue macrophage homeostasis. *Immunity* **56**, 516–530.e9 (2023).
18. K. Mehla, P. K. Singh, Metabolic regulation of macrophage polarization in cancer. *Trends Cancer.* **5**, 822–834 (2019).
19. S. H. Møller, P. C. Hsueh, Y. R. Yu, L. Zhang, P. C. Ho, Metabolic programs tailor T cell immunity in viral infection, cancer, and aging. *Cell Metab.* **34**, 378–395 (2022).
20. G. Liu, K. Yang, S. Burns, S. Shrestha, H. Chi, The $S1P_1$-mTOR axis directs the reciprocal differentiation of T_H1 and T_{reg} cells. *Nat. Immunol.* **11**, 1047–1056 (2010).
21. G. Liu, S. Burns, G. Huang, K. Boyd, R. L. Proia, R. A. Flavell, H. Chi, The receptor $S1P_1$ overrides regulatory T cell-mediated immune suppression through Akt-mTOR. *Nat. Immunol.* **10**, 769–777 (2009).
22. B. Ogretmen, Sphingolipid metabolism in cancer signalling and therapy. *Nat. Rev. Cancer* **18**, 33–50 (2018).
23. M. F. Rütti, S. Richard, A. Penno, A. von Eckardstein, T. Hornemann, An improved method to determine serine palmitoyltransferase activity. *J. Lipid Res.* **50**, 1237–1244 (2009).
24. Y. Wang, Y. Niu, Z. Zhang, K. Gable, S. D. Gupta, N. Somashekarappa, G. Han, H. Zhao, A. G. Myasnikov, R. C. Kalathur, T. M. Dunn, C.-H. Lee, Structural insights into the regulation of human serine palmitoyltransferase complexes. *Nat. Struct. Mol. Biol.* **28**, 240–248 (2021).
25. D. L. Davis, K. Gable, J. Suemitsu, T. M. Dunn, B. W. Wattenberg, The ORMDL/Orm-serine palmitoyltransferase (SPT) complex is directly regulated by ceramide: Reconstitution of SPT regulation in isolated membranes. *J. Biol. Chem.* **294**, 5146–5156 (2019).
26. S. G. Moreno, Depleting Macrophages In Vivo with Clodronate-Liposomes. *Methods Mol. Biol.* **1784**, 259–262 (2018).
27. M. Guilliams, C. L. Scott, Liver macrophages in health and disease. *Immunity* **55**, 1515–1529 (2022).
28. X. Zhang, X. Huang, J. Xu, E. Li, M. Lao, T. Tang, G. Zhang, C. Guo, X. Zhang, W. Chen, D. K. Yadav, X. Bai, T. Liang, NEK2 inhibition triggers anti-pancreatic cancer immunity by targeting PD-L1. *Nat. Commun.* **12**, 4536 (2021).
29. S. K. Biswas, Metabolic reprogramming of immune cells in cancer progression. *Immunity* **43**, 435–449 (2015).
30. T. Meyer, R. Fox, Y. T. Ma, P. J. Ross, M. W. James, R. Sturgess, C. Stubbs, D. D. Stocken, L. Wall, A. Watkinson, N. Hacking, T. R. J. Evans, P. Collins, R. A. Hubner, D. Cunningham, J. N. Primrose, P. J. Johnson, D. H. Palmer, Sorafenib in combination with transarterial chemoembolisation in patients with unresectable hepatocellular carcinoma (TACE 2): A randomised placebo-controlled, double-blind, phase 3 trial. *Lancet Gastroenterol. Hepatol.* **2**, 565–575 (2017).
31. A. Kuo, T. Hla, Regulation of cellular and systemic sphingolipid homeostasis. *Nat. Rev. Mol. Cell Biol.* **25**, 802–821 (2024).
32. S. Baweja, A. Kumari, P. Negi, A. Tomar, D. M. Tripathi, A. K. Mourya, A. Rastogi, P. D. Subudhi, S. Thangariyal, G. Kumar, J. Kumar, G. S. Reddy, A. K. Sood, C. Vashistha, V. Sarohi, C. Bihari, R. Maiwall, S. K. Sarin, Hepatopulmonary syndrome is associated with low sphingosine-1-phosphate levels and can be ameliorated by the functional agonist fingolimod. *J. Hepatol.* **79**, 167–180 (2023).
33. S. J. Priceman, S. Shen, L. Wang, J. Deng, C. Yue, M. Kujawski, H. Yu, S1PR1 is crucial for accumulation of regulatory T cells in tumors via STAT3. *Cell Rep.* **6**, 992–999 (2014).

34. Z. Xu, T. Ikuta, K. Kawakami, R. Kise, Y. Qian, R. Xia, M. X. Sun, A. Zhang, C. Guo, X. H. Cai, Z. Huang, A. Inoue, Y. He, Structural basis of sphingosine-1-phosphate receptor 1 activation and biased agonism. *Nat. Chem. Biol.* **18**, 281–288 (2022).
35. T. Muthusamy, T. Cordes, M. K. Handzlik, L. You, E. W. Lim, J. Gengatharan, A. F. M. Pinto, M. G. Badur, M. J. Kolar, M. Wallace, A. Saghatelian, C. M. Metallo, Serine restriction alters sphingolipid diversity to constrain tumour growth. *Nature* **586**, 790–795 (2020).
36. A. Asrir, C. Tardiveau, J. Coudert, R. Laffont, L. Blanchard, E. Bellard, K. Veerman, S. Bettini, F. Lafouresse, E. Vina, D. Tarroux, S. Roy, I. Girault, I. Molinaro, F. Martins, J. Y. Scoazec, N. Ortega, C. Robert, J. P. Girard, Tumor-associated high endothelial venules mediate lymphocyte entry into tumors and predict response to PD-1 plus CTLA-4 combination immunotherapy. *Cancer Cell* **40**, 318–334.e9 (2022).
37. K. B. Lorvik, B. Bogen, A. Corthay, Fingolimod blocks immunosurveillance of myeloma and B-cell lymphoma resulting in cancer development in mice. *Blood* **119**, 2176–2177 (2012).
38. C. Zhu, T. Kalincik, D. Horakova, Z. Zhou, K. Buzzard, O. Skibina, R. Alroughani, G. Izquierdo, S. Eichau, J. Kuhle, F. Patti, F. Grand'Maison, S. Hodgkinson, P. Grammond, J. Lechner-Scott, E. Butler, A. Prat, M. Girard, P. Duquette, R. A. L. Macdonell, B. Weinstock-Guttman, S. Ozakbas, M. Slee, M. J. Sa, V. van Pesch, M. Barnett, B. van Wijmeersch, O. Gerlach, J. Prevost, M. Terzi, C. Boz, G. Laureys, L. van Hijfte, A. G. Kermode, J. Garber, B. Yamout, S. J. Khoury, D. Merlo, M. Monif, V. Jokubaitis, A. van der Walt, H. Butzkueven, MSBase Study Group, Comparison between dimethyl fumarate, fingolimod, and ocrelizumab after natalizumab cessation. *JAMA Neurol.* **80**, 739–748 (2023).
39. M. M. Francis, T. A. Hummer, E. Liffick, J. L. Vohs, N. F. Mehdiyoun, A. C. Visco, Z. Yang, R. J. Kovacs, Y. Zhang, A. Breier, Effects of fingolimod, a sphingosine-1-phosphate (S1P) receptor agonist, on white matter microstructure, cognition and symptoms in schizophrenia. *Brain Imaging Behav.* **15**, 1802–1814 (2021).
40. C. Albert, J. Mikolajczak, A. Liekfeld, S. K. Piper, M. Scheel, H. G. Zimmermann, C. Nowak, J. Dörr, J. Bellmann-Strobl, C. Chien, A. U. Brandt, F. Paul, O. Hoffmann, Fingolimod after a first unilateral episode of acute optic neuritis (MOVING) - preliminary results from a randomized, rater-blind, active-controlled, phase 2 trial. *BMC Neurol.* **20**, 75 (2020).
41. I. Diouf, C. B. Malpas, S. Sharmin, I. Roos, D. Horakova, E. Kubala Havrdova, F. Patti, V. Shaygannejad, S. Ozakbas, S. Eichau, M. Onofrj, A. Lugaresi, R. Alroughani, A. Prat, P. Duquette, M. Terzi, C. Boz, F. Grand'Maison, P. Sola, D. Ferraro, P. Grammond, B. Yamout, A. Altintas, O. Gerlach, J. Lechner-Scott, R. Bergamaschi, R. Karabudak, G. Iuliano, C. McGuigan, E. Cartechini, S. Hughes, M. J. Sa, C. Solaro, L. Kappos, S. Hodgkinson, M. Slee, F. Granella, K. de Gans, P. A. McCombe, R. Ampapa, A. van der Walt, H. Butzkueven, J. L. Sánchez-Menoyo, S. Vucic, G. Laureys, Y. Sidhom, R. Gouider, T. Castillo-Trivino, O. Gray, E. Aguera-Morales, A. al-Asmi, C. Shaw, T. M. al-Harbi, T. Csepany, A. P. Sempere, I. Treviño Frenk, E. A. Stuart, T. Kalincik, Effectiveness of multiple disease-modifying therapies in relapsing-remitting multiple sclerosis: Causal inference to emulate a multiarm randomised trial. *J. Neurol. Neurosurg. Psychiatry* **94**, 1004–1011 (2023).
42. S. Teymouri, S. Pourbayram Kaleybar, S. S. Hejazian, S. M. Hejazian, K. Ansarin, M. Ardalan, S. Zununi Vahed, The effect of fingolimod on patients with moderate to severe COVID-19. *Pharmacol. Res. Perspect.* **11**, e01039 (2023).
43. X. Zhang, M. Lao, H. Yang, K. Sun, Y. Dong, L. He, X. Jiang, H. Wu, Y. Jiang, M. Li, H. Ying, X. Liu, J. Xu, Y. Chen, H. Zhang, R. Zhou, J. Gao, X. Bai, T. Liang, Targeting cancer-associated fibroblast autophagy renders pancreatic cancer eradicable with immunochemotherapy by inhibiting adaptive immune resistance. *Autophagy* **20**, 1314–1334 (2024).
44. T. Nguyen, J. Du, Y. C. Li, A protocol for macrophage depletion and reconstitution in a mouse model of sepsis. *STAR Protoc.* **2**, 101004 (2021).

Acknowledgments

Funding: This work was supported by the National Key Research and Development Program of China 2024YFA1306400 (X.B. and X. Lu), the National Natural Science Foundation of China U20A20378 (T.L.), the National Natural Science Foundation of China U23A20462 (X.B.), the National Natural Science Foundation of China 82403852 (Xiaozhen Zhang), the National Science and Technology Major Project 2024ZD0524900 (X. Lu), the "Ling Yan" Research and Development Program of Department of Zhejiang Province Science and Technology 82071867 (X.B.), the Natural Science Foundation of Zhejiang Province LQN25H160036 (Xiaozhen Zhang), the Natural Science Foundation of Zhejiang Province LQ22H160044 (Xiaoyu Zhang), the China Postdoctoral Science Foundation 2024 T170810 (Xiaozhen Zhang), and the China Postdoctoral Science Foundation 2024 M752879 (Xiaozhen Zhang). **Author contributions:** Conceptualization: Xiaozhen Zhang, X. Lu, X.B., and T.L. Methodology: Xiaozhen Zhang, M.L., K.S., L.L., L.H., J.S., and X. Lu. Resources: Xiaozhen Zhang, K.S., H.Y., C.G., and Xiaoyu Zhang. Investigation: Xiaozhen Zhang, M.L., K.S., H.Y., X. Li., S.Z., S.W., and Xiaoyu Zhang. Visualization: Xiaozhen Zhang, M.L., H.Y., L.H., L.L., and S.Z. Data curation: Xiaozhen Zhang, M.L., and C.G. Validation: Xiaozhen Zhang, M.L., H.Y., L.L., and S.W. Formal analysis: Xiaozhen Zhang, S.Z., and J.S. Software: Xiaozhen Zhang, M.L., K.S., and L.H. Supervision: Xiaozhen Zhang, X. Lu, X.B., and T.L. Funding acquisition: Xiaozhen Zhang, Xiaoyu Zhang, X. Lu, X.B., and T.L. Project administration: X.B. and T.L. Writing—original draft: Xiaozhen Zhang and X. Lu. Writing—review and editing: Xiaozhen Zhang, D.X., X. Lu, X.B., and T.L. **Competing interests:** The authors declare that they have no competing interests. **Data and materials availability:** All data and code to understand and assess the conclusion of this research are present in the paper, the Supplementary Materials, SRA database, GEO database, and PRIDE database (The accession number for the RNA-seq in this paper is PRJNA1143706; the accession number for the scRNA-seq in this paper is GSE275911; the accession number for phosphoproteomics in this paper is PXD054708).

Submitted 3 December 2024
Accepted 16 April 2025
Published 21 May 2025
10.1126/sciadv.adv0558